UNIVERSIDADE FEDERAL DE PERNAMBUCO
DEPARTAMENTO DE FÍSICA - CENTRO DE CIÊNCIAS EXATAS E DA NATUREZA
PROGRAMA DE PÓS-GRADUAÇÃO EM FÍSICA

MATHEUS VALENÇA CORREIA

Effects of three-body interactions on structural phases of classical two-dimensional clusters

Recife
2021

MATHEUS VALENÇA CORREIA

Effects of three-body interactions on structural phases of classical two-dimensional clusters

Dissertation presented to the Postgraduate program of the Physics Department of the Federal University of Pernambuco as a partial requirement to obtain the degree of Master in Physics.

Supervisor: Clécio Clemente de Souza Silva

Program of studies: Theoretical and Computational Physics

Recife

2021

Catalogação na fonte
Bibliotecária Nataly Soares Leite Moro, CRB15-861

C824e Correia, Matheus Valença
Effects of three-body interactions on structural phases of classical two-dimensional clusters / Matheus Valença Correia. – 2021.
68 f.: il., fig., tab.

Orientador: Clécio Clemente de Souza Silva.
Dissertação (Mestrado) – Universidade Federal de Pernambuco. CCEN, Física, Recife, 2021.
Inclui referências e apêndice.

1. Theoretical and computational physics. 2. Three-body interactions. 3. Classical clusters. 4. Charged colloids. I. Silva, Clécio Clemente de Souza (orientador). II. Título.

530.1 CDD (23. ed.) UFPE- CCEN 2021 - 132

MATHEUS VALENÇA CORREIA

EFFECTS OF THREE-BODY INTERACTIONS ON STRUCTURAL PHASES OF CLASSICAL TWO-DIMENSIONAL CLUSTERS

Dissertação apresentada ao Programa de Pós-Graduação em Física da Universidade Federal de Pernambuco, como requisito parcial para a obtenção do título de Mestre em Física.

Aprovada em: 29/06/2021.

BANCA EXAMINADORA

_____

Prof. Clécio Clemente de Souza Silva
Orientador
Universidade Federal de Pernambuco

_____

Prof. Leonardo Ribeiro Eulálio Cabral
Examinador Interno
Universidade Federal de Pernambuco

_____

Prof. Mauro Melchiades Dória
Examinador Externo
Universidade Federal do Rio de Janeiro

AGRADECIMENTOS

Aos meus pais, Ana Paula e Ubiratan, e à minha irmã, Manuella, pelas referências desde cedo, pelo carinho que sempre dedicaram a mim e pelas condições que me ofereceram para que concluísse essa etapa.

Ao meu orientador, Clécio, pela gentileza, paciência e habilidade para lidar com seu orientando e com a pesquisa.

A Anna Letícia, pelo amor e tranquilidade que sempre consegue me transmitir.

Aos meus amigos de departamento e para vida, Marquinhos, Ricardo, Lucas Gabriel, Hugo, Emily, Nicolas e outros que sempre compartilharam café e conversas no DF ou na cantina de Deda.

Aos meus amigos e companhias da Várzea, Kivia, Henrique, Clara, Ewelim, Anny e Rodrigo, pelos encontros no Terraço e pelas conversas na Praça da Várzea e arredores.

Ao meu grupo do laboratório, professor Leonardo Cabral, Daniel, Fillipe, José, Rubens, Raí e Emerson, pela companhia e por todas as ajudas e discussões importantes (ou não).

Ao CNPq, pelo financiamento desta pesquisa, à Universidade Federal de Pernambuco, pública e de qualidade, e a todos os funcionários do seu Departamento de Física.

ABSTRACT

When a physical system has many interacting constituents, many-body terms will arise in the Hamiltonian, besides the usual two-body interactions. These terms are often ignored in numerical studies due to their high computational cost. However, many-body terms are responsible for important corrections in charged colloidal systems and promote structural changes in clusters of Abrikosov vortices in superconductors. The main goal of this work is to determine the effect the addition of a three-body term has on the properties of two-dimensional clusters of classical interacting particles. In order to understand such effect, we carried out semi-analytical calculations and numerical minimization of the system free energy, using a simulated annealing scheme based on the Langevin dynamics. We considered N particles ($3 \leq N \leq 50$) confined in a parabolic potential and interacting via a pair potential. We considered three of the most studied pair potentials: logarithmic, Coulomb and Yukawa. The novelty in our study consisted in the addition of a short-ranged Gaussian three-body interaction potential with tunable amplitude. The obtained configurations were compared with the typical case in which the particles interact only via a pair potential. In this last situation, we recover the typical concentric rings of particles, widely found in the literature. With the addition of the three-body interaction, our findings include changes in the ring occupation numbers and the emergence of a first-order like transition associated with the bistability phenomenon due to the competition between the two- and three-body potentials. This transition is accompanied by a sudden cluster compaction, especially in the $N > 20$ range, for all two-body potentials, and a phase separation effect starting around $N = 40$, in which the initial single cluster was divided into smaller ones. These results indicate that the three-body term in the interaction potential of many confined particles can induce dramatic changes in the equilibrium configurations and, therefore, should not be ignored in those particle systems.

Keywords: three-body interactions; classical clusters; charged colloids; superconducting vortices.

RESUMO

Sistemas físicos com um grande número de componentes podem apresentar, além das interações usuais de dois corpos, contribuições de três, quatro ou mais corpos no Hamiltoniano. Frequentemente, esses termos de muitos corpos são ignorados em estudos numéricos devido ao alto custo de processamento que normalmente acarretam. No entanto, termos de muitos corpos são responsáveis por diversas correções de interesse em colóides carregados e também pela modificação estrutural de aglomerados de vórtices de Abrikosov em supercondutores. O objetivo deste trabalho é determinar o efeito do termo de três corpos nas propriedades de aglomerados bidimensionais de partículas clássicas interagentes. Para isso, realizamos estudos semi-analíticos e a minimização numérica da energia livre do sistema, utilizando um procedimento de recozimento (*annealing*) simulado baseado na dinâmica de Langevin. Foram consideradas N partículas ($3 \leq N \leq 50$) confinadas em um potencial parabólico e interagindo repulsivamente por meio de um potencial repulsivo de dois corpos. Alguns dos mais estudados potenciais de dois corpos foram considerados: logarítmico, Coulomb e Yukawa. A novidade deste trabalho consistiu em adicionar um potencial atrativo de três corpos Gaussiano de curto alcance, com intensidade variável. Os resultados foram comparados com o caso típico, quando as partículas interagem somente através do potencial de dois corpos. Nessa condição, obtivemos os típicos arranjos de partículas em anéis concêntricos, já amplamente registrados pela literatura. Com a adição da interação de três corpos, nossos achados incluíram a modificação dos números de ocupação dos anéis e o surgimento de uma transição do tipo primeira ordem associado ao fenômeno de biestabilidade devido à competição entre os potenciais de dois e três corpos. Essa transição foi acompanhada por uma abrupta compactação do sistema, especialmente para $N > 20$, em todos os potenciais de dois corpos, e um efeito de separação de fase a partir de $N = 40$, em que o aglomerado único foi dividido em outros menores. Esses resultados mostram que o termo de três corpos no potencial de interação de muitas partículas confinadas pode produzir mudanças dramáticas nas configurações de equilíbrio. Portanto, trata-se de contribuição que não deve ser ignorada nesses sistemas de partículas.

Palavras-chaves: interações de três corpos; agregados clássicos de partículas; colóides carregados; vórtices supercondutores.

LIST OF FIGURES

LIST OF TABLES

CONTENTS

1 INTRODUCTION

A plethora of different interactions are established in the study of Physics. In the undergraduate education, we usually discuss the so-called pairwise interactions, or two-body interactions, such as the Coulomb potential for charged point particles. In such cases, the interactions are evaluated for a pair of interacting entities. These contributions are added up to obtain the total potential energy of the system. However, this is not a full description of many physical systems. Sometimes the sum of all pairwise interactions is not equal to the total energy, especially in dense systems. Indeed, according to Louis (2002) we can not completely describe any known material in nature only by using two-body potentials. For instance, even noble gases require a three-body potential to describe triple-dipole interactions (AXILROD; TELLER, 1943).

If we consider a system of N interacting particles, many-body (or non-additive) effects may arise. Usually, we need to describe the Hamiltonian of such systems with a interaction potential written as

$$U(\{\boldsymbol{r}_i\}) = \sum_{i<j}^{N} U_{2b}(r_{ij}) + \sum_{i<j<k}^{N} U_{3b}(r_{ij}, r_{jk}, r_{ik}) + \sum_{i<j<k<l}^{N} U_{4b}(r_{ij}, r_{jk}, r_{kl}, r_{il}) + ... \qquad (1.1)$$

where r_{ij} is the distance between particles i and j, U_{2b} is a two-body interaction, U_{3b} is a three-body interaction, U_{4b} is a four-body interaction and higher many-body terms are omitted. The sum is made for all available pairs, trios and quartets of particles in the system.

For illustration purposes, Figure 1 compares the two- and three-body interactions among a given (i, j, k) triple of interacting particles. The two-body interactions are counted in pairs (for example, between particles i and j, separated by r_{ij}). If we consider central potentials, which are spherically symmetrical (or circularly symmetrical, for two-dimensional systems), the three-body term in the Eq. 1.1 depends only on the relative distances between the particles in a given triple, which are shown in Figure 1. The three-body interaction appears when the three particles are within the range of the interaction, which happens especially when a large density of particles are considered, since the average inter-particle distance becomes smaller.

The three-body potentials play an important role in different areas of Physics, such as in the nuclear, atomic and condensed matter (GUO; GASPARIAN, 2018). For clarification purposes, we make a distinction between effective and fundamental three-body forces. The Earth-Moon system is an example of a system possessing tidal forces, which can be considered effective three-body forces. This is the case if we consider that the bodies of water on the Earth surface are under the main gravitational influence of the planet, however they are affected by the movement of a nearby third body, the Moon. The effect is actually a result of the combination of three gravitational two-body potentials, such as the first term of Equation 1.1, and not a pure three-body potential (second term of Equation 1.1). For a given set of three bodies

Figure 1 – Schematic comparison between two-body and three-body interactions in a given set of interacting particles.

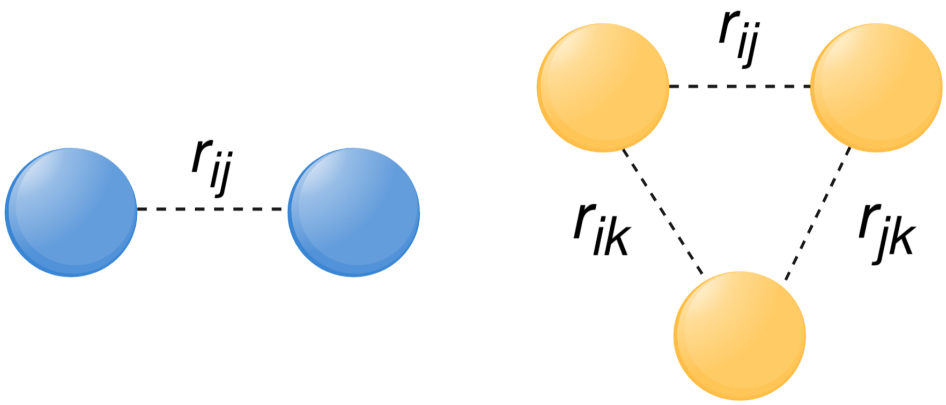

Source: The author (2020).

interacting gravitationally, this equates the following potential energy

$$\mathcal{U} = -\frac{Gm_1m_2}{|\mathbf{r}_1 - \mathbf{r}_2|} - \frac{Gm_2m_3}{|\mathbf{r}_3 - \mathbf{r}_2|} - \frac{Gm_3m_1}{|\mathbf{r}_3 - \mathbf{r}_1|}, \tag{1.2}$$

where G is the gravitational constant and m_i and r_i are the mass and position of the i-th body.

In nuclear systems, on the other hand, there are models informing the presence of three-body forces in the form of U_{3b} (Equation 1.1). Primakoff and Holstein (1939) showed that the description of nuclear systems only by using two-body potentials is a bad approximation. In light nuclei, for example, considering the available scattering data, three-body interactions may be responsible for up to one fifth of the binding energy (PIEPER; WIRINGA, 2001). One of the first of these fundamental three-body nucleon potentials, $V_{(3)}$, was proposed by Fujita and Miyazawa in 1957. It is such that $V_{(3)} = V(123) + V(231) + V(312)$ and

$$V(ijk) \propto \frac{\exp(-r_{ij})}{r_{ij}} \frac{\exp(-r_{jk})}{r_{jk}}, \tag{1.3}$$

where r_{ij} is the distance between two nucleons i and j. $V_{(3)}$ is physically associated with a pion exchange process: a initial particle emits a pion, which is scattered by a second particle and, then, absorbed by a third (FUJITA; MIYAZAWA, 1957). The pion exchanges are the mechanism behind the long-range parts of the nuclear strong force, which is further developed in Hammer, Nogga and Schwenk (2013).

An important issue with potentials in the form of U_{3b} is the computational cost which they bring in numerical studies, since we need to account for all available trios of particles, which grows much faster than the number of pairs when we increase the number of constituents. Going beyond a mere small corrections of the energy, these potentials can actually cause important changes in the properties of many systems. For example, it may generate new spatial

patterns in superconducting vortices and change the boundaries of the colloidal crystals phase diagram. In this work, we aim to investigate what structural changes that the addition of a monotonic three-body potential can cause in particle arrangements of confined interacting particles. These classical systems are important models for mesoscopic systems and are vastly studied in the presence of two-body interacting potentials alone.

It has been verified by numerical studies that the presence of competing interactions in these confined systems can generate a diversity of new complex spatial patterns. Usually, these interactions are non-monotonic pair potentials, which are composed of an attractive and a repulsive parts. This motivates us to investigate if a monotonic two-body repulsive potential combined with a three-body attractive interaction can cause relevant effects as well. In such situation, we performed Molecular Dynamics simulations and analytical calculations to investigate changes in the equilibrium states of classical two-dimensional clusters of particles.

This dissertation is organized as follows. In chapter 2, we review some aspects of two-dimensional confined clusters of particles and the presence of competing interactions as cause for important structural changes in these systems. Also, the three-body interaction in charged colloids suspensions and vortices in superconductor is approached. Chapter 3 summarizes the numerical model we adopt to study classical two-dimensional clusters in the presence of a three-body potential. In Chapter 4, we exhibit the results of our simulations, detecting important changes in the shell structure and the appearance of a discontinuity in the energy first derivative resembling a first-order transition and that is linked to a phase separation effect of the particle clusters.

2 A REVIEW ON CLASSICAL 2D CLUSTERS AND THREE-BODY INTERACTIONS IN COLLOIDS AND VORTEX SYSTEMS

2.1 2D CLUSTERS OF PARTICLES WITH MONOTONIC PAIR INTERACTIONS

The confinement of classical interacting particles in two dimensions is a extensively studied model for some mesoscopic systems. Cândido et al. (1998) and Jean, Even and Guthmann (2001) indicate relevant examples of mesoscopic systems whose properties are assimilated by these particle clusters: polymer colloids confined between glass plates, mesoscopic superconductors, confined ions cooled by laser traps and electrons confined in quantum dots. Jean, Even and Guthmann (2001) point that experiments of mesoscopic systems leads to common difficulties, such as the tuning of the number of interacting particles or the confinement amplitude. These are examples of relevant parameters easily tuned by confined 2D clusters.

The main goals of such confined systems include the determination of the particle distribution in the ground-states and in the metastable states and the phase transitions the system may undergo. J.J. Thomson initially studied theses systems in his classical model for the structure of the atom (THOMSON, 1904). As he was unable to obtain analytical solutions for three-dimensional atoms at the time, Thomson assumed electrons interacted via Coulomb potential and were restricted to a plane. More specifically, they arranged themselves in concentric rings. The Thomson procedure was based on adding particles in a ring as much as a stability criteria allowed and then place the rest in the centre, in order to establish a shell structure. Since then, many numerical and experimental studies were performed with modifications of this Thomson problem, adopting a diversity of inter-particle and confinement potentials.

A simple experimental realization of such systems, the macroscopic Wigner islands[1], can be found in Jean, Even and Guthmann (2001). Using an easily tunable experimental setup, composed essentially by charged steel balls, a metallic circular frame and loudspeakers, the authors were able to reproduce a mesoscopic system which have a parabolic confinement and logarithmic inter-particle interaction under a given temperature, simulated by mechanical shaking. Figure 2 exhibits some of the equilibrium configurations obtained by Jean, Even and Guthmann (2001), where we can observe the formation of concentric shells, with an increasing number of rings as we increase the number of particles.

By using a similar procedure such as Thomson, Partoens and Peeters (1997) developed a numerical study of "classical" two-dimensional atoms using Monte Carlo simulations, studying how the particle shells are affected by a power law confinement and submitted to a repulsive potential. The following dimensionless Hamiltonian described the system

$$H = \sum_{i=1}^{N} r_i^n + \sum_{j>i}^{N} \frac{1}{|\vec{r}_i - \vec{r}_j|^{n'}}. \tag{2.1}$$

[1] Confined clusters of N of particles are the finite N limit for the 2D Wigner crystal, which forms a triangular lattice for $N \to \infty$.

Figure 2 – Equilibrium configurations obtained for several number of confined particles by using the macroscopic Wigner islands setup.

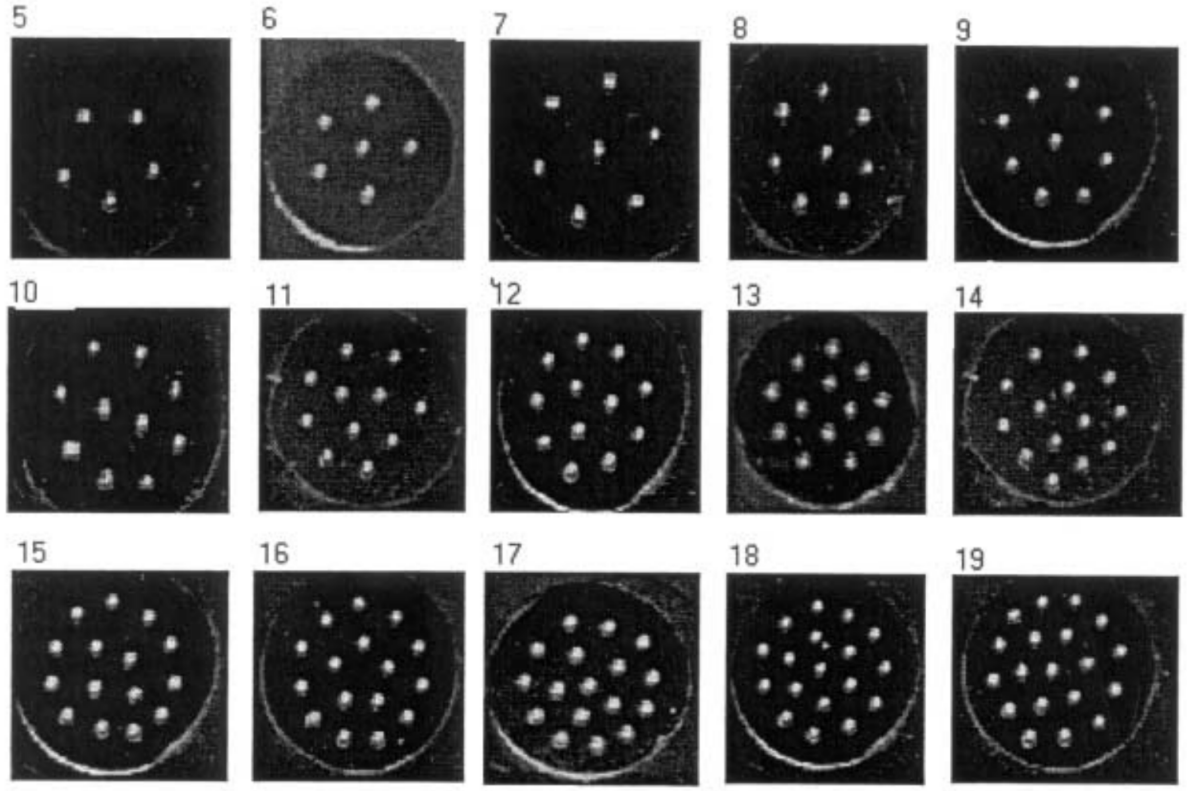

Source: Jean, Even and Guthmann (2001).

Eq. 2.1 is a typical Hamiltonian in the study of confined particles. The first term is the confinement potential, where a large n ($n \approx 10$) is associated with a hard-wall confinement. The second term is the pair inter-particle potential, where $|\vec{r}_i - \vec{r}_j|$ denotes the distance between a pair of particles and $n' = 1$ recovers the Coulomb potential expression. The literature uses different confinement and inter-particle potentials for the confined systems. In this case, the authors studied different cases of n and n' for N interacting particles and reproduced the typical shell structures. They detected that the maximum number of particles that each ring supports increases with respect to the power law coefficient n (Figure 3, left) and decreases in relation to the inter-particle potential coefficient n' (Figure 3, right). Also, it was found that for the typical case of a parabolic confinement ($n = 2$) there are normal modes which are independent of N and whose values depend on the functional form of the inter-particle potential. Finally, Partoens and Peeters were able to build a "classical" Mendeeleev table, summarizing all the ring structure results they found for different N, n and n'.

The shell occupation and the structural form of confined two-dimensional particle clusters can be modified by the variation of parameters of interest. Kong, Partoens and Peeters (2003) numerically investigate a system with N particles submitted to a parabolic confinement and a screened Coulomb (Yukawa) inter-particle potential with the following dimensionless Hamil-

Figure 3 – In the left, the maximum number of particles allowed in a ring according to different power law coefficients (n) of confining potentials. In the right, the same is evaluated for different inter-particle potentials with power law coefficient n'. n and n' are observed in Eq. 2.1.

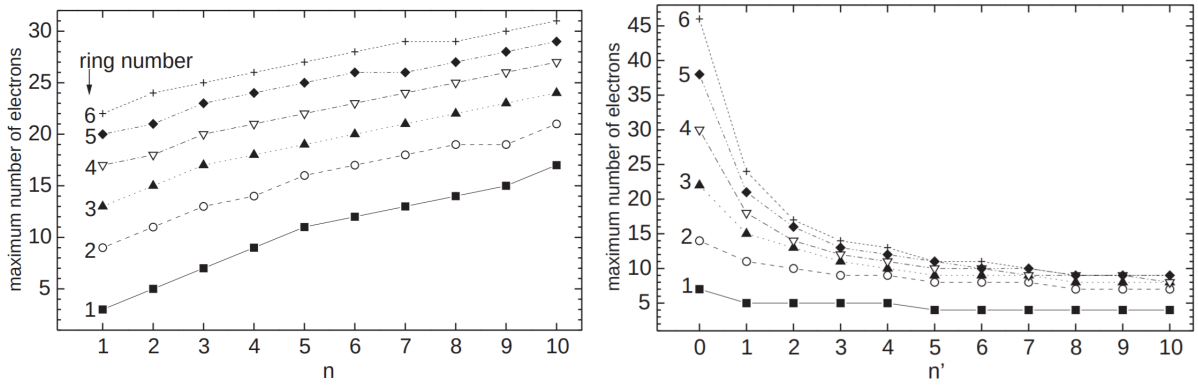

Source: Partoens and Peeters (1997).

tonian

$$H = \sum_{i}^{N} r_i^2 + \sum_{j>i}^{N} \frac{\exp\left(-\kappa r_{ij}\right)}{r_{ij}}, \tag{2.2}$$

where r_{ij} is the distance between two given particles and κ is the screening parameter. Small κ ($\kappa < 1$) defines a long-ranged repulsive inter-particle interaction, the opposite (short-ranged interaction) occurring for $\kappa \approx 10$.

With the variation of κ, the authors observed small differences in the ring occupation numbers for $N < 30$ (small clusters), however for many values of N the structures are not sensitive to the value of κ. Figure 4A shows the energy and appearance of the $N = 19$ ground-state as κ is increased. For a given range of κ, the $(1, 6, 12)$ configuration do not have the lowest energy, but the $(1, 7, 11)$ does. Also, the circular shells are replaced by an hexagonal structure in the high-κ limit. For increasing κ, the energy decreases and so the configuration radius. The particles, then, experience a smaller confinement energy in the central region, forming the hexagonal pattern as observed in the correspondent infinite system.

For large N, topological defects are detected and their position in the arrangement also depends on κ. For $N = 300$, Figure 4B shows the Voronoi diagrams of $\kappa = 0.25$, 2.0 and 16.0 indicating the position of such defects (in dark grey color) in the configurations of Kong, Partoens and Peeters (2003). The relative position of the defects is compared with other pure inter-particle potentials, such as the logarithmic, dipole ($\propto \frac{1}{r^3}$) and Coulomb. The melting temperature of the system is also affected by the variation of κ. For small clusters, in the high-κ limit the melting temperature T_m decreases, while for a large cluster of particles it can increase. Figure 4C shows such behavior of T_m for $N = 19$, $N = 20$ and $N = 300$.

Figure 4 – A and B: structural changes due to variation of κ parameter for small and large clusters. C: Melting temperature of particle clusters with respect to κ.

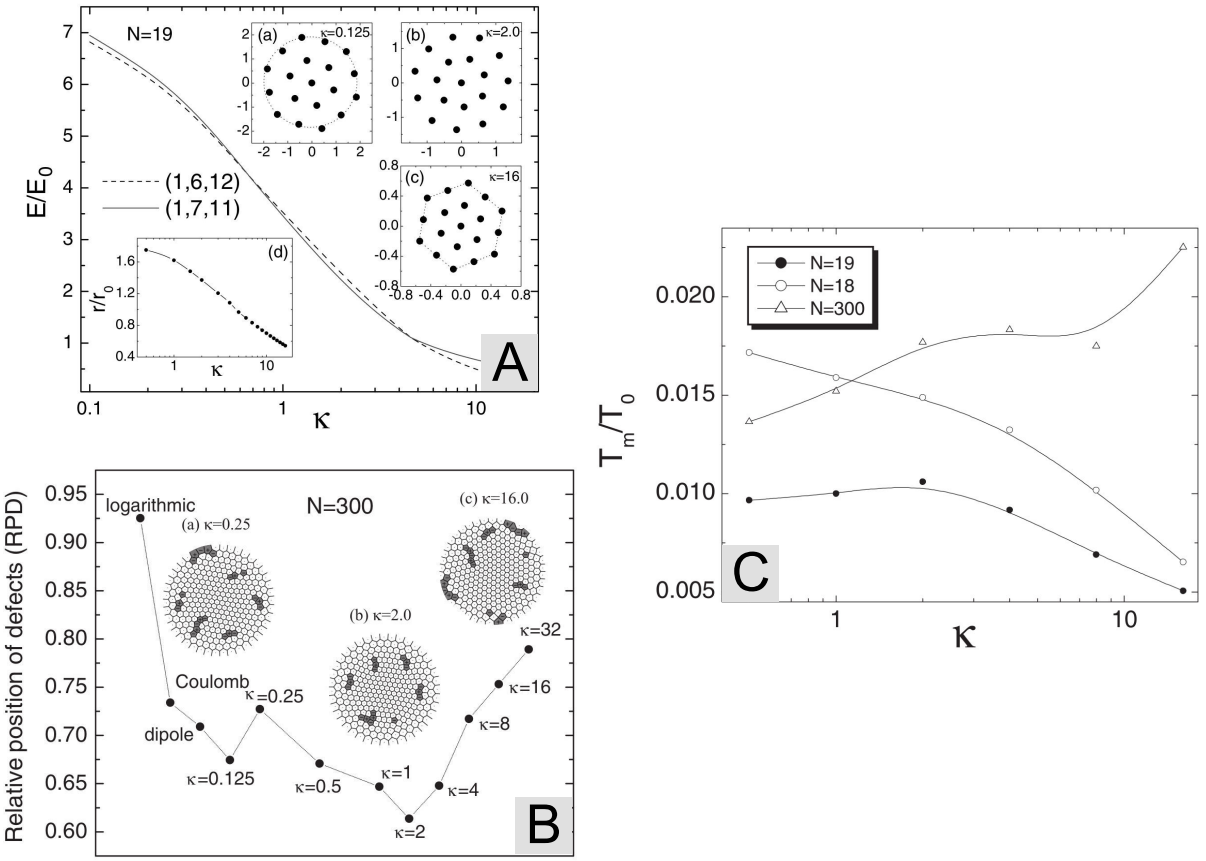

Source: Kong, Partoens and Peeters (2003).

2.2 2D CLUSTERS OF PARTICLES WITH COMPETING INTERACTIONS

The clusters of particles which we exhibited so far have a pure monotonic repulsive inter-particle potential (Coulomb and screened Coulomb/Yukawa). However, an interesting feature of some physical systems is the presence of competing interactions of different scales in the inter-particle potential. Examples of such systems are given by Liu, Chew and Yu (2008): colloids with the addition of polymers (where an attractive force is induced by the polymers and a repulsive one is due to charged colloidal particles) and magnetic materials (short-ranged exchange and long-range dipole interactions).

Competing interactions give rise to important and rich spatial patterns in some model systems beyond the domain of confined clusters. An example is found in the Molecular Dynamics study of Reichhardt and Bishop (2010), which uses a non-monotonic pair interaction combining a long-range Coulomb and a short-range Yukawa terms. According to the density and the temperature of the system, which are tunable, the authors are able to find multiple arrangements in the infinite system, as shown in Figure 5: clumps of particles, stripes, bubbles and an hexagonal lattice can be identified.

Figure 5 – Variety of phases in a system with competing interactions. Each point represents a particle in the simulation box.

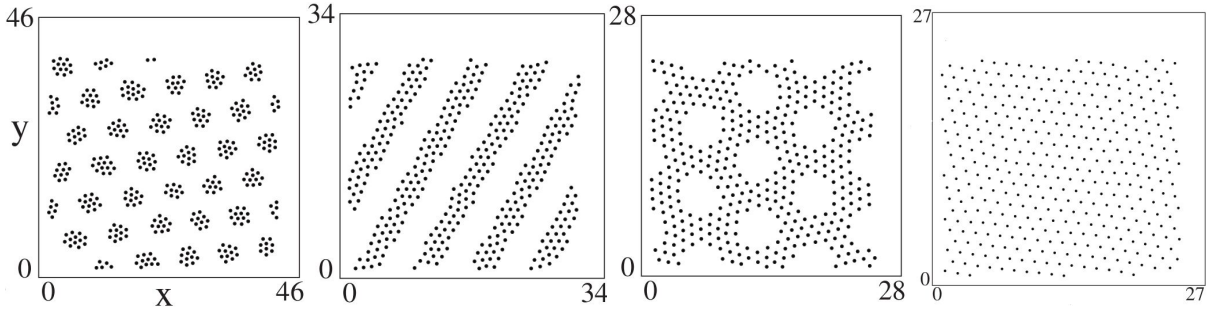

Source: Reichhardt and Bishop (2010).

In confined systems, the competing interactions also play an important role in the particles self-assembly. Now we highlight one of the many recent works dealing with competing interactions in confined clusters of particles. In 2008, Liu, Chew and Yu (2008) worked on a two-dimensional parabolic confinement and the following non-monotonic inter-particle potential

$$U_{ij} = q^2 \frac{\exp(-\alpha r_{ij})}{r_{ij}} - B\exp(-\beta r_{ij}), \tag{2.3}$$

where q is the particle charge and r_{ij} is the distance between two particles. The first term is a repulsive screened Coulomb (Yukawa) potential, which recovers the Coulomb expression setting $\alpha = 0$. The second term is an attractive interaction. α and β are the parameters controlling the screening length of both terms. B is responsible for the strength of the attractive part.

In this work, Liu, Chew and Yu (2008) reproduce the typical shell structure of particles. However, by varying α, β and B, they also obtain a wide variety of complex configurations, some of which can be seen in Figure 6 for 250 particles. Besides the traditional shell structure, we highlight the formation of smaller clusters of particles (Figure 6, d1-d3), concentric stripes (Figure 6, c2-c4) and void structures (Figure 6, b3-b4). According to the authors, these patterns are a direct consequence of the competition "among the inter-particle repulsive and attractive forces as well as the confinement force acting on the particles in minimizing the total system energy" (LIU; CHEW; YU, 2008).

Another interesting and recent work by Xu et al. (2021) studies non-equilibrium patterns in the dynamics of a system with logarithmic confinement and non-monotonic inter-particle interaction. The correspondent two-body force is given by

$$F\left(r_{ij}\right) = \frac{1}{r_{ij}^2} - Be^{-Cr_{ij}} \tag{2.4}$$

The first term corresponds to a Coulomb repulsion. B controls the relative amplitude of attraction to repulsive parts and $1/C$ is the screening length for the attraction term. The latter can have multiple physical correspondents. For example, holes in layered transition metal oxides

Figure 6 – Equilibrium configurations observed in the two-dimensional space parameter of α, B for a confined system with 250 particles and the competing inter-particle interactions of Eq. 2.3.

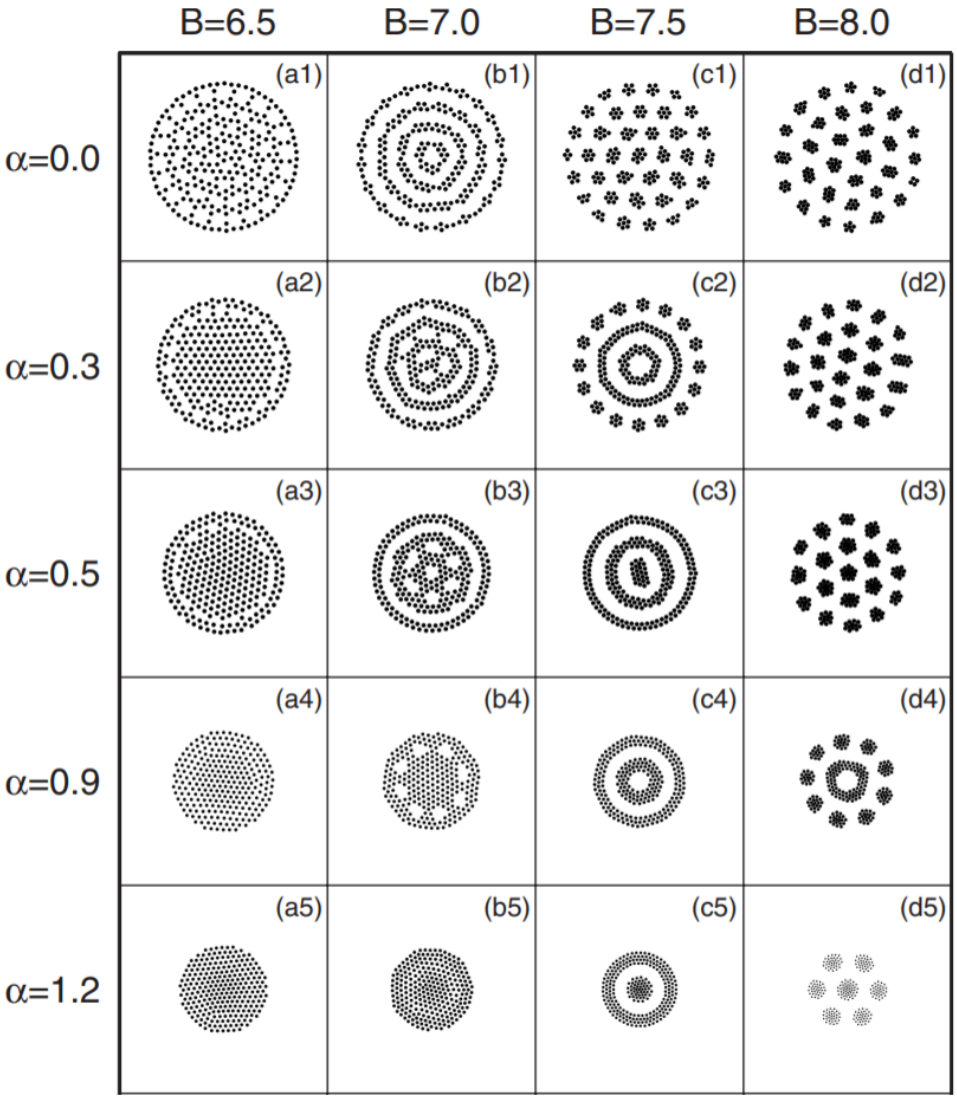

Source: Liu, Chew and Yu (2008).

interact via Coulomb repulsion and short-range exponential attractive terms. The authors also explain that this model can be used to study colloids and charged-dust systems.

The confinement potential has the following form

$$V(r) = -\beta\, ln(R - r), \tag{2.5}$$

where β is the confining potential strength and R is the radius of confinement. The adopted procedure is based on a quickly decrease of β, that is, a quench in the confining potential. This produces a non-equilibrium state equivalent to a particle "explosion" which generate multiple spatial patterns when the system reaches a new equilibrium. Figure 7 shows two cases for the quickly decrease of β. At $t = 0$, after a simulated annealing, an equilibrium configuration is obtained. The confining potential amplitude is, then, suddenly decreased from $\beta = 15.1$ to $\beta = 2.0$ for $R = 50$ (Figure 7, first row) and from $\beta = 15.1$ to $\beta = 0.1$ for $R = 65$ (Figure

7, second row). The authors observe the cluster expansion with a multi-step dynamics and the changing of the shell structure into a stripe pattern or into small clusters organized in a ringlike structure in the new equilibrium state.

Figure 7 – Quenching of the logarithmic confining potential in a particle cluster with competing two-body interactions. At $t = 0$, the sudden decrease of confinement strength β occurs from $\beta = 15.1$ to $\beta = 2.0$ (first row) and confinement radius $R = 50$. Second row show the same situation from $\beta = 15.1$ to $\beta = 0.1$ (second row).

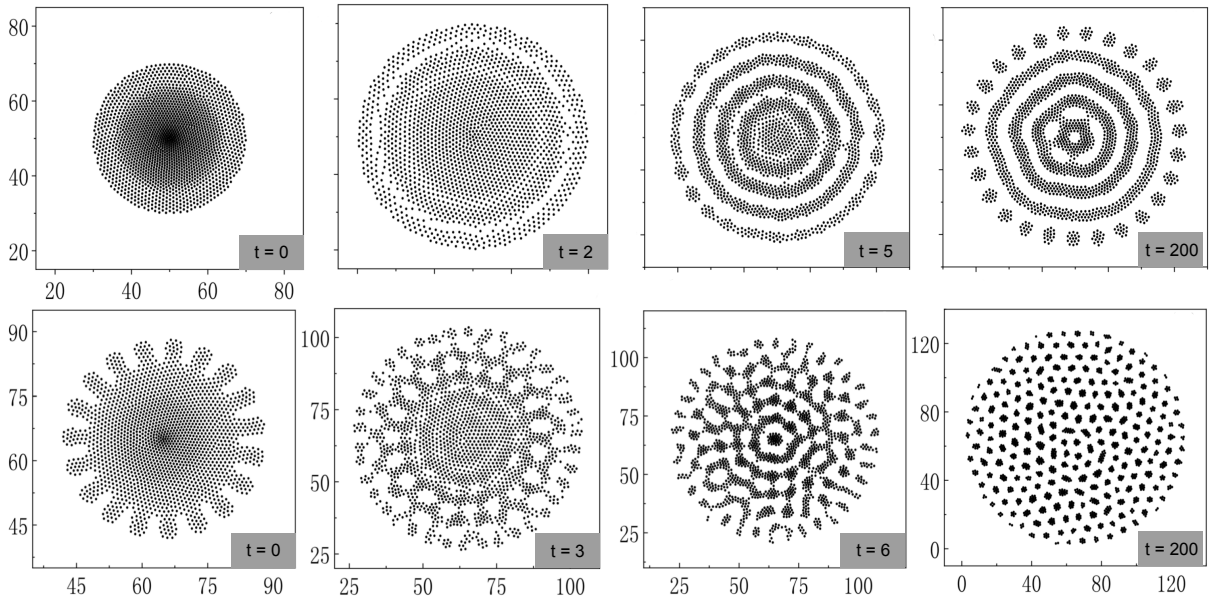

Source: Xu et al. (2021).

2.3 THREE-BODY INTERACTIONS IN PHYSICAL SYSTEMS

2.3.1 Colloidal suspensions

A first example of the effect of the three-body potential is the colloidal suspensions. Colloids were first systematically studied by Thomas Grahan in 1861. He observed a solution which did not diffuse through a semipermeable membrane, as the component molecules (colloidal particles) were too large for that (DHONT, 1996). Common colloidal particles range from $1\,nm$ to $10\,\mu m$ in size. Colloids are, then, suspensions or dispersions of a substance (dispersed phase) in some other continuous phase, typically liquids. According to these phases, respectively, we found multiple examples of known colloids (Figure 8), such as milk (liquid-liquid), liquid aerosols (liquid-gas), gelatin (liquid-solid) and the whipped cream[2] (gas-liquid).

Two interactions are always present among colloidal particles distanced by r, the hard-core repulsion and the van der Waals attraction. The hard-core repulsion simply results from the fact that two particles cannot overlap and it is modelled considering an infinite potential for $r \leq D$

[2] Also known as the Chantilly cream.

Figure 8 – Different examples of colloids: milk is an emulsion, sneezes and coughing contain aerosols, gelatin is a known gel and Chantilly is a foam.

Source: From left to right: Pexels (2020), the American Centers for Disease Control and Prevention (CDC) (2019), Wikimedia Commons (2019) and Cooking Classy (2019).

and zero for $r > D$. The attractive van der Waals force has its origins in the attraction between temporary molecule dipoles (MORBIDELLI; AROSIO, 2016) and, in the context of colloids, has received a macroscopic approach by two works of Hamaker: Hamaker (1937) and Hamaker (1938). The author wanted to evaluate the van der Waals interaction for two spherical colloidal particles of radius a_1 and a_2. With a suitable integration of London's dispersion equation

$$V_{vw}(r) = -\int_{V_1} dv_1 \int_{V_2} dv_2 \, \frac{q^2 \lambda}{r^6}, \tag{2.6}$$

where q is the particle charge, λ is the London-van der Waals constant, dv_i and V_i is the volume element and total volume of the i-th particle, it is possible to obtain

$$V_{vw}(r) = -\frac{A}{6}\left[\frac{2a_1a_2}{r^2-(a_1+a_2)^2} + \frac{2a_1a_2}{r^2-(a_1-a_2)^2} + \ln\left(\frac{r^2-(a_1+a_2)^2}{r^2-(a_1-a_2)^2}\right)\right], \tag{2.7}$$

where $A = \pi^2 q^2 \lambda$ is the Hamaker constant. A is usually positive, meaning that van der Waals force is attractive. This expression can be reduced at small r (decaying with first power of distance) or large r (decaying with the sixth power, recovering typical van der Waals behavior).

Colloidal particles (the macroions) can also be charged, which happens because the particles itself carry charged chemical groups or additional charged polymers are attached to their surface, in order to stabilize the suspension (DHONT, 1996). This superficial charge distribution attracts nearby microions of opposite charge in the electrolyte and establishes the formation of a spherically symmetric ionic double layer around the colloidal particle (Figure 9, left). These ionic distributions are responsible for the "screening" of the electrostatic interaction between colloidal surface charges, which is described by a Yukawa-type (screened Coulomb) U_Y potential such that

$$U_Y \propto \frac{\exp(-\kappa r)}{r} \tag{2.8}$$

where κ^{-1} is the Debye–Hückel screening length, which is proportional to the double layer width. Also, it is possible to add salt in the colloidal suspensions in order to control the κ

parameter and, then, the double layer width. Usually, when an electrolyte is present, the double layer is smaller than the average interparticle distance (VERWEY, 1999).

Figure 9 – In the left, the double layer formed around charged colloidal particles. In the right, the plot of the DLVO potential (green solid curve), a sum of the van der Waals (red curve) and the double layer Yukawa (blue curve) interactions.

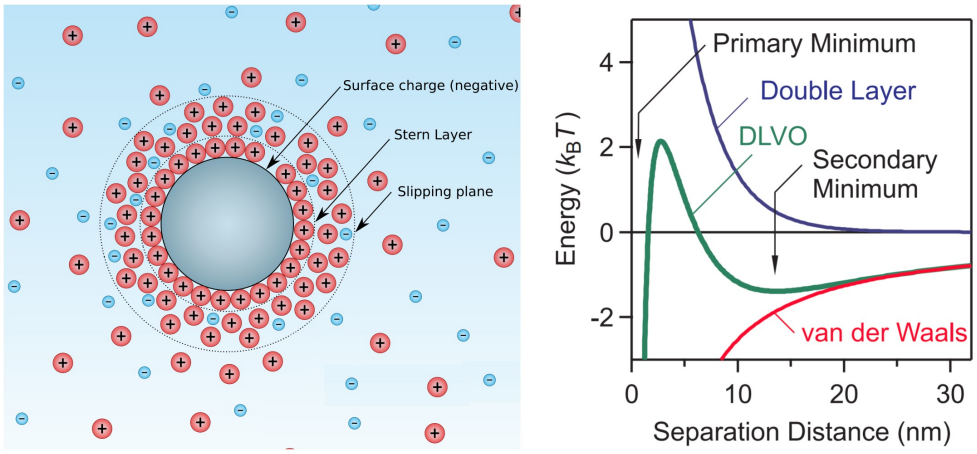

Source: Wikimedia Commons (2012) and Trefalt and Borkovec (2014), respectively.

The combination of interactions 2.7 and 2.8 is known as the DLVO[3] theory, a standard description of charged-stabilized colloidal suspensions. In stable colloids, the particles remain dispersed and do not aggregate or sediment. The DLVO potential, which is a result of the combinations of Eqs. 2.7 and 2.8, is shown in the right part of Figure 9.

It is known that colloidal systems can undertake phase transitions (for instance, they can crystallize and melt (DHONT, 1996)) and, as expected from Section 2.3.2 considerations, the role of inter-particle interaction is important in defining the phase diagram of such systems (IACOVELLA et al., 2010). In a numerical study with the use of the Poisson-Boltzmann model, Dobnikar et al. (2003) observed the existence of many-body interactions that can change the melting point of colloidal crystals.

The approach of Dobnikar et al. (2003) was based on the evaluation of an effective pair potential, U_{eff}. In general, effective potentials are used to bypass the manipulation of many-body terms, although they lead to some thermodynamic inconsistencies in some calculations (LOUIS, 2002). According to Dobnikar et al. (2003), it can be shown that there is a unique mapping between $U_{eff}(r, \rho)$ and the pair correlation function of a liquid, $g(r)$, at density ρ of the colloidal system. $g(r)$ informs how the density varies along the distance r with respect to some reference particle. In other words, we can interpret how the density varies along the system only by using U_{eff}. The special point is that the dependence on ρ arises due to many-body interactions in the system, since a true pair potential (U_{2b}) alone cannot account for all these contributions. Thus, if any dependence on the density ρ is detected in U_{eff}, a

[3] DLVO stands for the works of (Boris) Derjaguin and (Lev) Landau, (Evert) Verwey and (Theodoor) Overbeek.

difference is established between U_{eff} and U_{2b}, reveling the existence of many-body terms in the Hamiltonian.

Dobnikar et al. (2003) noticed that there is a discrepancy (Figure 10, left) between U_{eff} and the DLVO potential in high density, low-salt suspensions. The low-salt condition corresponds to the case in which $d_m\kappa \approx 1$, where d_m corresponds to the average separation between colloidal particles and, thus, the ionic double layer extends itself at this same order of length. The different behavior observed is a faster decay of U_{eff} in comparison to the Yukawa potential which, according to the authors, is motivated by the presence of many-body forces. This deviation was not observed in the high-salt regime, where the behavior follows the typical Yukawa interaction (solid line, Figure 10, left).

Dobnikar et al. (2003) wanted to translate this shift in the behavior of U_{eff} into a pure Yukawa system, so they model this deviation as a truncation in the Yukawa pair potential. A smaller cutoff distance better replicates the low-salt regime. Physically, this truncation corresponds to the breaking of bonds between the colloidal particles and its neighbors. Considering this representation, they observed the melting of the colloidal crystal at lower temperatures, as they truncate the potential at smaller distances (Figure 10, right), namely for a cutoff ranging from 3.07 to 1.35 units of length. The latter value corresponds to a region between the first and second neighbor shells.

Figure 10 – Left: Effective force curves in colloidal crystals with different salt concentrations (dotted lines). A difference in the behavior is observed in the low-salt regime ($d_m\kappa \approx 1$), where the force decays faster than the Yukawa interaction in the DLVO theory (solid line). Right: Change in colloidal crystal melting line when a truncated Yukawa potential is adopted. Each line of numerical data indicate the distance for truncation and $\lambda \propto \kappa^{-1}$.

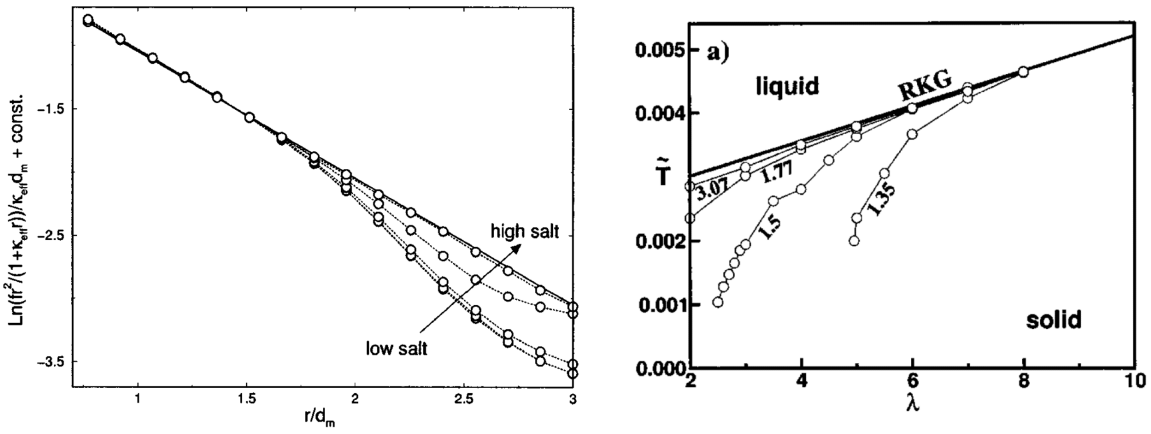

Source: Dobnikar et al. (2003).

The specific many-body contributions to the colloidal crystals were not possible to be determined by Dobnikar et al. (2003). In the following year, however, Dobnikar et al. (2004) directly measured three-body interactions in systems with 3 colloids and find it to be attractive and with range comparable to the Yukawa potential. The authors used an optical tweezer trap, inserting each particle at a time in the arrangement, in order to evaluate the particle position distributions, the pair potential and, then, the three-body contributions. The difference between

the total energy and the sum of pairwise interactions (Yukawa potential) for the trio is shown in the right part of Figure 11. The positive values observed especially around the colloidal particles correspond to the manifestation of an attractive three-body contribution which is responsible for lowering the total interaction energy.

Also, the authors explained the mechanism of this nonpairwise interaction in low-salt, high density colloids. In this regime, the double layer of Figure 9 extends over a wide distance in the suspension, affecting the local ionic distribution and the electrostatic interaction between colloids. We can consider the interaction of colloids, say A and B, which are sufficiently far apart. Under the influence of a nearby third colloidal particle C, the ionic clouds may interact with each other, disturbing the pair repulsion. Then, the interaction between A and B becomes dependent on the position of C, which gives rise to the three-body contribution.

Figure 11 – In the left, experimental setup of three trapped (by means of optical tweezers) silica particles of $990\,nm$ suspended in water. Particles are distanced by $r = 2.5\,\mu m$ and $d = 1.6\,\mu m$. In the right, a heat map of the difference between total electrostatic energy and the sum of three pairwise interactions (Yukawa potential). Positive difference values indicate the presence of an attractive three-body energy term, especially in the red areas. Horizontal and vertical directions indicate y and x axes, respectively.

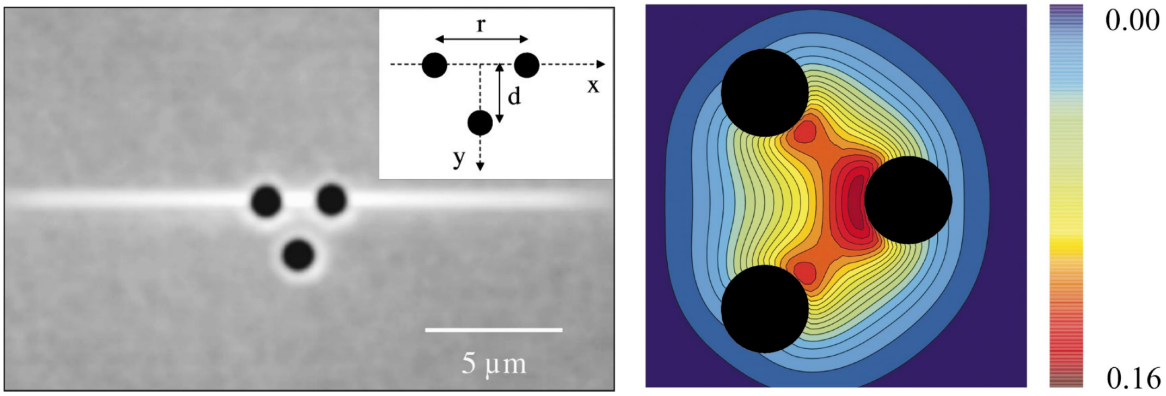

Source: Dobnikar et al. (2004).

One last point should be made to address the usefulness of colloidal suspensions in the direct measure of these many-body effects. Tuning two- and three-body interactions separately is an experimental challenge (BUCHLER; MICHELI; ZOLLER, 2007), especially in nuclear and atomic systems, where positional information is usually not accessible. Colloids, however, allow us at least to turn the three-body interaction off simply by the addition of salt, as has been observed in the behavior of low- and high-salt suspensions (DOBNIKAR et al., 2003). This allows us to qualify the colloids as ideal systems to study the influence of these non-linear contributions in the behavior of interacting physical constituents.

2.3.2 Vortices in superconductors

Another system of interest for three-body interactions are the magnetic vortices in superconductors. The superconductivity was discovered by Kamerlingh Onnes around 1911, when he verify the abrupt disappearance of resistivity (perfect electrical conduction) in some metals in very low temperatures and below critical values of an external magnetic field (TINKHAM, 1996). Vortices arise in a superconductor as normal (non-superconducting) regions which may appear inside the sample, where superconducting currents circulate around to establish a separation between normal and superconducting region (KITTEL, 1996). Inside the vortices, a quantized magnetic flux is established.

In the context of the Ginzburg-Landau (GL) phenomenological theory, an important classification associated to single-band superconductors employs the GL parameter $\kappa = \frac{\lambda}{\xi}$, a ratio between the penetration length λ and the coherence length ξ of the superconductor. The former is a measure of the usual magnetic field penetration inside the superconductor and the latter is the typical length in which the order parameter (ψ) varies. $|\psi|^2$ is directly associated with the density of superconducting electrons (TINKHAM, 1996).

Type-1 (type-2) superconductors exhibit a ratio such that $\kappa < \frac{1}{\sqrt{2}}$ ($> \frac{1}{\sqrt{2}}$). This classification is associated with differences in their magnetic response and vortex states. Usually, through the mechanism of the Meissner effect, an external magnetic field H is expelled from the inside of a superconductor sample. If H reaches a value above H_{c1} (Figure 12), it penetrates the superconductor and then superconductivity in type-1 systems is destroyed. Vortex state is not stable in type-1 system, but it is shown that vortex-vortex interaction in type-1 slabs would be attractive at small distances between the vortices, as described by calculations in Kramer (1971). According to Gladilin et al. (2015), as a result of such attraction, vortices can often merge into a multiquanta domain of many shapes.

In type-2 superconductors, for $H_{c1} < H < H_{c2}$[4] (Figure 12), H can partially penetrate the sample by means of singly-quantized magnetic flux, the vortices, still maintaining a superconducting region around them. Vortex-vortex interaction is known to be purely repulsive in type-2 superconductors. Thus, they pack and organize themselves in a stable hexagonal (Abrikosov) lattice inside the sample (Figure 13), and can also be found as liquid and as a glass (LING et al., 2001).

Also, with a modification in the GL free energy, several works also consider multicomponent superconductors, which goes beyond the GL parameter categorization, as they are formed by electrons from different energy bands (EDSTROM, 2012). In particular, there is a current discussion on two-component superconductors, formed by a type-1 and a type-2 systems, allowing non-monotonic two-body vortex competing interactions: short-range repulsive, but long-range attractive. The competition of such interactions of different ranges results in structural changes in the equilibrium configurations of the vortex state, when compared to

[4] H_{c1} and H_{c2} are known as the first and second critical fields. (TINKHAM, 1996)

Figure 12 – Examples of magnetization curves for type-1, type-2 and type-1.5 superconductors.

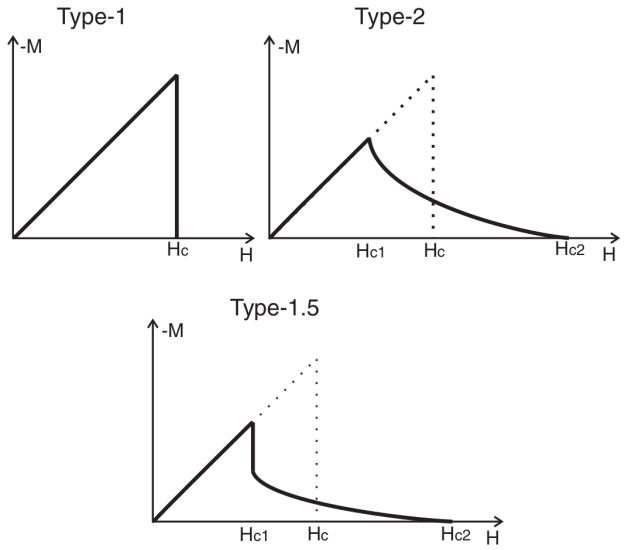

Source: Carlström, Garaud and Babaev (2011).

Figure 13 – Left: representation of superconductor vortices organized in a triangular lattice for temperature $T = 0$. Right: scanning-tunneling-microscope observation of the hexagonal vortex lattice in a type-2 superconductor ($NbSe_2$) at low temperature ($1.1\,K$).

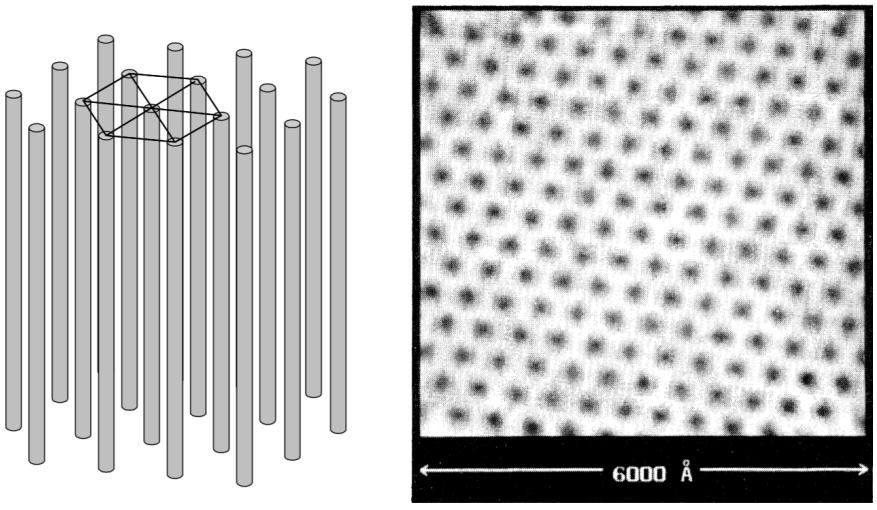

Source: Silva (2003) and Hess et al. (1989), respectively.

single-component materials. This class of superconductors was first described experimentally in Moshchalkov et al. (2009). The authors obtain, through Bitter decoration technique, surprising stripe and gossamerlike vortex structures in a MgB_2 superconductor sample. The results, which are shown in Figure 14, are confirmed by molecular dynamic simulations and compared with a typical vortex lattice in a $NbSe_2$ type-2 superconductor (Figure 14, b and d).

A few years ago, it has been discussed by numerical studies (CARLSTRÖM; GARAUD; BABAEV, 2011) that nonpairwise interactions also appear in type-1.5 systems and are relevant to the

Figure 14 – Bitter decoration images of type-1.5 MgB_2 superconductor sample (a), showing a stripe vortex pattern, and the vortex lattice (b) of a $NbSe_2$ type-2 superconductor. The samples were submitted to a $5Oe$ magnetic field. (c) and (d) show Molecular Dynamics simulation reproduce such results.

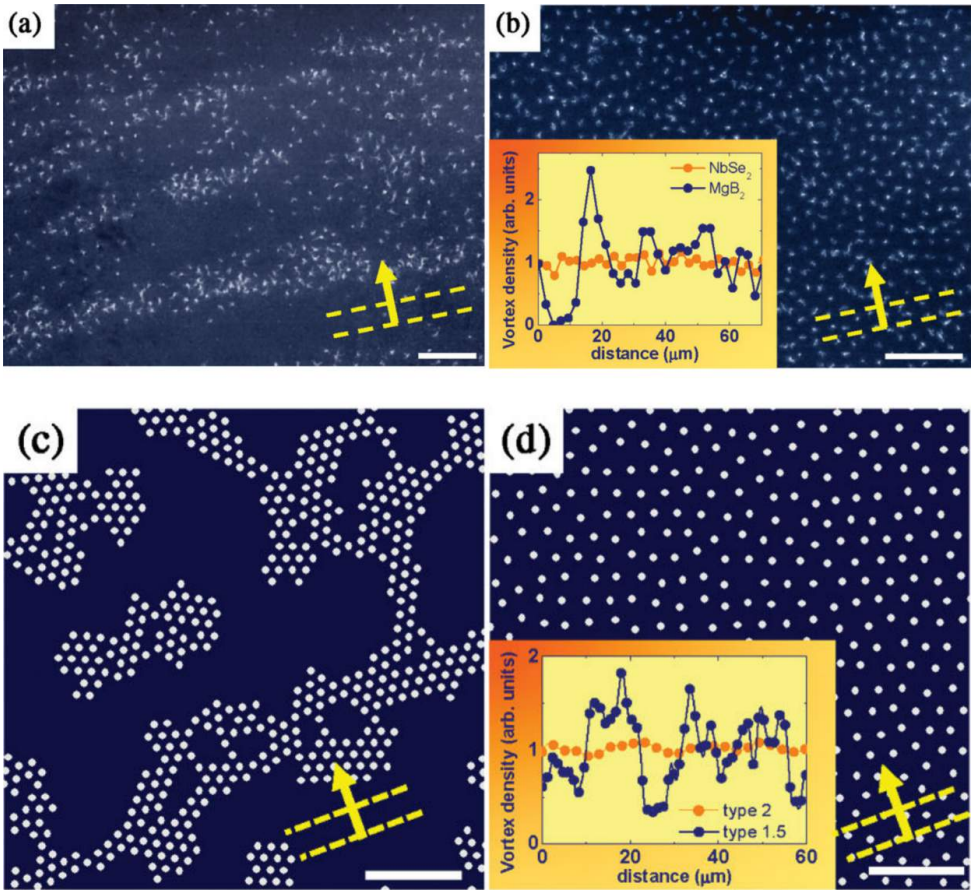

Source: Moshchalkov et al. (2009).

formation of highly disordered vortex states which could not be formed only by considering the sum of two-body intervortex forces. Figure 15 shows the influence of the three-body interaction in multivortex structures in a Josephson-coupled multilayer of type-1 and type-2 superconductors. In this case, the stripelike configuration (Fig. 15, center), with a strong coupling enabled, is not accessible by the non-monotonic two-body interaction alone, which is axial-symmetric. In fact, the final state is the result of repulsive multibody forces among vortices. Carlström, Garaud and Babaev (2011) also detect the breaking of the large cluster into smaller clusters, when considering a diluted initial cluster configuration of 30 vortices (Fig 15, right). During the energy minimization process, if only two-body forces were considered, the initial cluster would contract in order to minimize the energy. However, due to many-body forces, it expands and then breaks into smaller clusters.

In Edström (2013), a numerical study is also carried out for type-1, type-2 and type-1.5 superconductors by the minimization of the GL free energy. A scheme of two or three vortices in fixed positions is used in order to obtain the energy map when an extra vortex is added to the system afterwards. This method does not account for small vortex-vortex distances. The

Figure 15 – Magnetic flux density of the ground state of different vortex equilibrium configurations in type-1.5 superconductor. In the left, system has a weak three-body interaction. Center and right: a strong three-body interaction (strong coupling). In the center, stripe-like configuration. In the right, small clusters obtained after the breaking of an initial dilute vortex cluster.

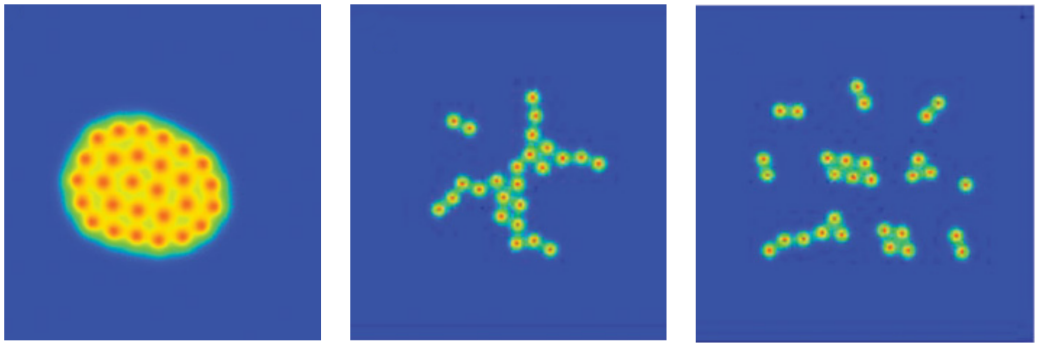

Source: Carlström, Garaud and Babaev (2011).

author used a free energy density of a two-component superconductor (type 1.5), excluding the second condensate term to consider one-component superconductors (for types 1 and 2). The main finding is a mismatch between the total interaction energy and the sum of the pairwise interactions. According to the author, this indicates the appearance of many-body forces, which he associates to three- and four-body terms.

Figure 16 exhibits the energy results, which indicate a repulsive three-body interaction for types 1 and 1.5 (Figure 16a,c) and a attractive one for type-2 (Figure 16b), which is compatible with observations in Carlström, Garaud and Babaev (2011). Except for a small region in type-1 (Figure 16a), three-body interaction is more significant than four-body's, but both are relevant in comparison with the pairwise interaction.

Figure 16 – Contribution of two-, three- and four-body terms in the energy as a function of R (in units of $\sqrt{2}\xi_1$, where ξ_1 is the coherence length of one of the condensates in the absence of coupling) of a single-component superconductor of types 1 and 2 and a two-component 1.5 sample.

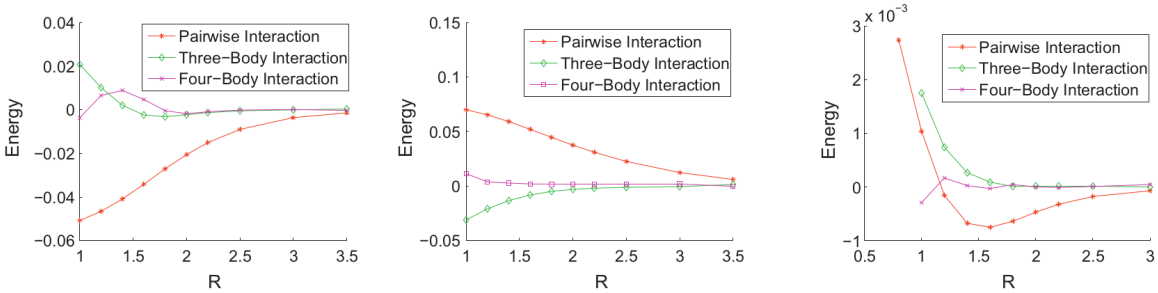

(a) Type-1. (b) Type-2. (c) Type-1.5.

Source: Edström (2013).

Section 2.3.1 and this one show that the presence of many-body contributions to charged colloids and vortex systems are important and lead to results which cannot be explained only by using pair interactions, even if we are considering non-monotonic pair potentials.

3 METHODOLOGY

In this chapter, we provide details of the theoretical model and numerical methods used in this work.

3.1 INTERACTION POTENTIALS AND THE CONFINEMENT

The two-dimensional particle system we study is composed of N point-like particles submitted to competing inter-particle interactions: a repulsive two-body potential U_{2b} and an attractive three-body potential U_{3b}, both depending only on the distances between the particles involved. The system is confined through an harmonic confinement potential U_{conf}, used to assemble particles in a limited region of two-dimensional space and has the form

$$U_{conf} = k_0 \sum_{i}^{N} r_i^2, \tag{3.1}$$

where k_0 is a constant which determines the confinement strength and r_i is the radial position of the i-th particle.

We adopt different functional forms for the U_{2b} potential: a logarithmic, a Coulomb-like and a Yukawa-like interaction. The Coulomb potential describes systems of charged particles. The Yukawa potential, which is basically the Coulomb interaction with the addition of an exponential decay term, was already mentioned in Chapter 2. It appears when charged spherical colloids are in suspension and interacting repulsively with each other. Logarithmic potential is associated, for example, with the interaction of magnetic vortices (separated by a distance $r << \lambda_L$)[1] in superconducting samples (TINKHAM, 1996), in which the interaction is proportional to $\log(\frac{1}{r}) = -\log(r)$ at small distances.

The functional forms of U_{2b} are, then, the following

$$U_{2b}(r_{ij}) = k_2 \begin{cases} -\sum_{i=1}^{N} \sum_{j=i+1}^{N} \log(r_{ij}) & \text{, if logarithmic} \\ \sum_{i=1}^{N} \sum_{j=i+1}^{N} \frac{1}{r_{ij}} & \text{, if Coulomb-like} \\ \sum_{i=1}^{N} \sum_{j=i+1}^{N} \frac{1}{r_{ij}} \exp\left(-\frac{r_{ij}}{\lambda}\right) & \text{, if Yukawa-like} \end{cases} \tag{3.2}$$

where $\boldsymbol{r}_i$ is the position vector of i-th particle, $r_{ij} = |\boldsymbol{r}_i - \boldsymbol{r}_j|$ is the distance between i-th and j-th particles and $k_2 > 0$ is a constant. The sum is made for all possible pairs of particles in a given N. The potential profiles are plotted in Figure 17, alongside the two-body forces,

[1] λ_L is the London penetration depth, a measure indicating the magnetic field penetration inside a superconductor sample.

obtained from U_{2b} using the identity $\boldsymbol{F}_{2b} = -\boldsymbol{\nabla} U_{2b}$. We observe, in the right plot, the different ranges in the two-body forces.

Figure 17 – Functional forms of U_{2b} potential (left) and correspondent two-body forces (right). In this case, $k_2 = \lambda = 1.0$.

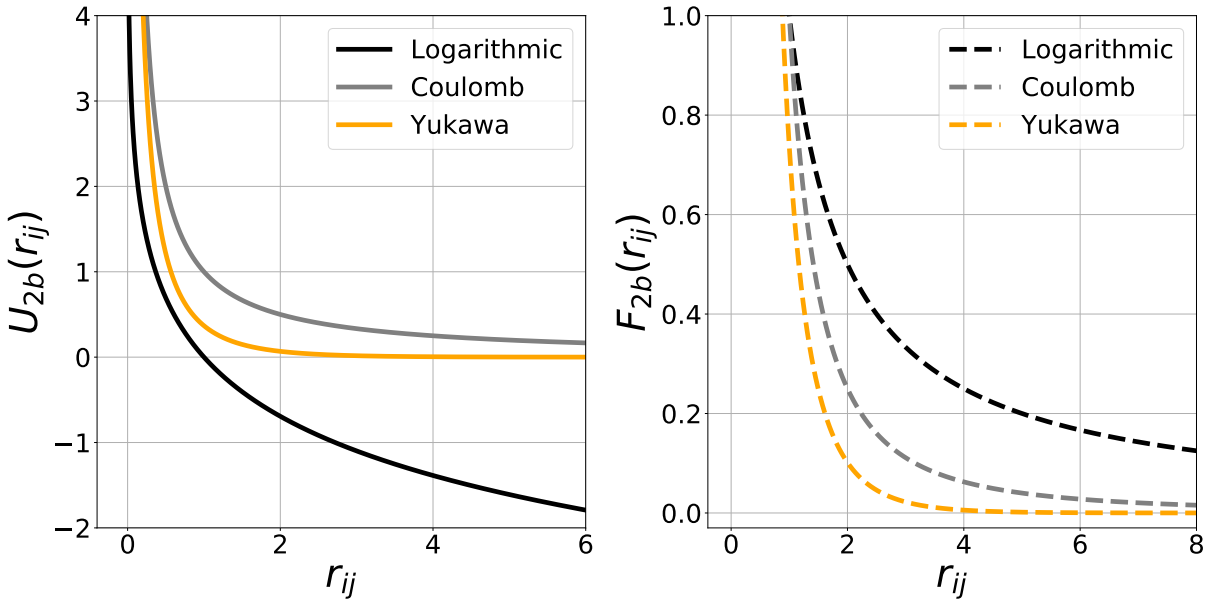

Source: The author (2020).

The three-body interaction is the main ingredient for the phenomena discussed. It emerges as three particles (and not a pair of them) are close enough to each other, if we consider distance-dependent potentials. In order to use a monotonic potential for three-body interaction (the same case for U_{2b}), we chose a Gaussian exponential form for U_{3b} as follows

$$U_{3b}(r_{ij}, r_{ik}, r_{jk}) = -k_3 \sum_{i=1}^{N} \sum_{j=i+1}^{N} \sum_{k=j+1}^{N} \exp\left(-\frac{r_{ij}^2 + r_{ik}^2 + r_{jk}^2}{2\xi^2}\right), \tag{3.3}$$

where k_3 is our main parameter controlling the strength of the three-body interaction, ξ is the Gaussian width (set to unity throughout this work) and the sum is made for all possible trios of (i, j, k) particles. Figure 18 shows plots for several values of k_3 and ξ, where we note a negative potential growing monotonically towards zero as $R = \sqrt{r_{ij}^2 + r_{ik}^2 + r_{jk}^2}$ grows for a given (i, j, k) trio.

In order to perform the simulations of confined particles, we can write the potential energy ($U = U_{conf} + U_{2b} + U_{3b}$) in a dimensionless form for each type of U_{2b}. The potential energy

Figure 18 – Three-body potential profiles for several values of k_3 and ξ. r_o is the unit of length.

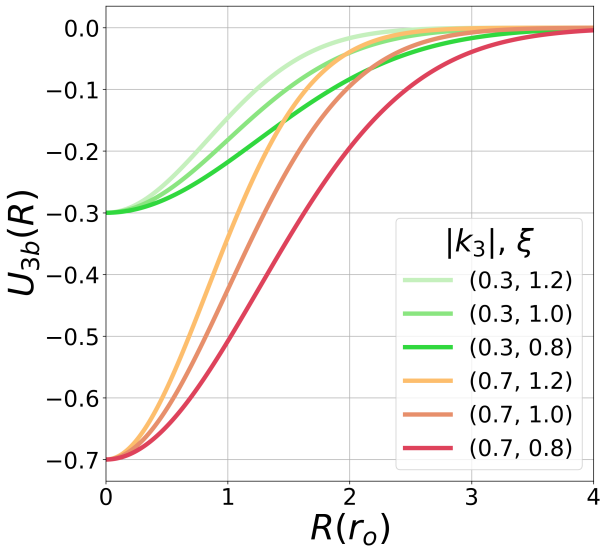

Source: The author (2020).

Figure 19 – In the left, trio of interacting particles submitted to U_{3b}. Particles are close enough to interact if all interparticle distances (r_{ij}, r_{ik} and r_{jk}) are equal or smaller than R_{3b}. In the right, the N-dependent relation of possible pairs and trios to be formed among particles, indicating the computational cost of the three-body interaction.

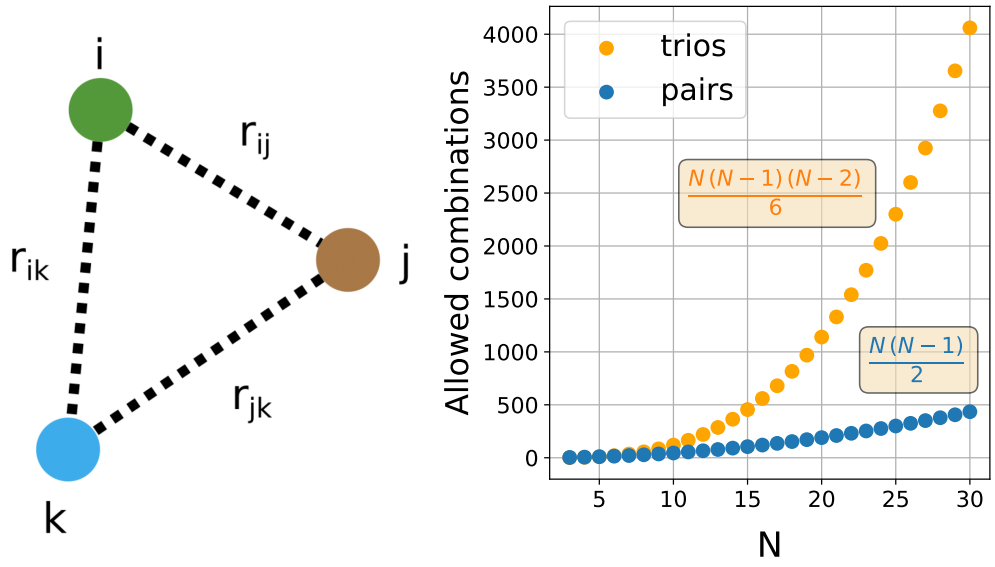

Source: The author (2021).

can be initially written as

$$U(r_{ij}, r_{ik}, r_{jk}) = k_0 \sum_{i}^{N} r_i^2 + k_2 \sum_{(i,j)}^{N} \begin{cases} -\log(r_{ij}) \\ \dfrac{1}{r_{ij}} \\ \dfrac{1}{r_{ij}} \exp\left(-r_{ij}\right) \end{cases} - k_3 \sum_{(i,j,k)}^{N} \exp\left(-\frac{r_{ij}^2 + r_{ik}^2 + r_{jk}^2}{2\xi^2}\right) \quad (3.4)$$

Considering Partoens and Peeters (1997) and taking the three-body potential into account, we can adopt the following units

$$r_o = \left(\frac{k_2}{k_o}\right)^{(2+n)^{-1}} \tag{3.5}$$

$$E_o = [(k_2)^2 (k_0)^n]^{(2+n)^{-1}} \tag{3.6}$$

$$F_o = [(k_2)(k_0)^{1+n}]^{(2+n)^{-1}} \tag{3.7}$$

for position coordinates, energy and force, respectively. Here, n is the power associated with the U_{2b} potential: $n = 0$ is the case for logarithmic and $n = 1$, Coulomb and Yukawa potentials. With these, we have the potential energy in the dimensionless form of

$$U(r_{ij}, r_{ik}, r_{jk}) = \sum_i^N r_i^2 + \sum_{(i,j)}^N \begin{cases} -\log(r_{ij}) \\ \dfrac{1}{r_{ij}} \\ \dfrac{1}{r_{ij}} \exp\left(-\dfrac{r_{ij}}{\lambda}\right) \end{cases} - k_3 \sum_{(i,j,k)}^N \exp\left(-\frac{r_{ij}^2 + r_{ik}^2 + r_{jk}^2}{2\xi^2}\right) \tag{3.8}$$

Since we are considering damped dynamics in our simulations, there is no kinetic energy in the system for $t >> 0$, so the potential energy (Eq. 3.8) is the only contribution in the Hamiltonian.

We can also adopt a numerical cutoff to avoid unnecessary calculations involving U_{3b}. Figure 19 illustrates the case: if each particle in a given trio is simultaneously separated from each other by a distance smaller than R_{3b}, then they define a trio that interact via U_{3b} and that will be considered in the algorithm. We adopt $R_{3b} = 4\, r_o$, which is a reasonable value since three particles equally distanced by this amount results in an extremely small contribution of U_{3b} to the total potential energy (Eq. 3.8): approximately $4 \times 10^{-11} E_o$, considering $k_3 = 1.0$ and $\xi = 1.0$. In the case of the three-body interaction, setting a cutoff radius is specially important, as the number of possible trios grows much faster in relation to N than pairs do, as the right part of Figure 19 shows. Each trio represents an extra iteration step to be considered in the algorithm, so the appropriate use of R_{3b} contributes to save computational time.

3.2 MOLECULAR DYNAMICS AND THE LANGEVIN EQUATION

We make use of the molecular dynamics (MD) algorithm to simulate and obtain equilibrium arrangements in two dimensions, revealing us some dynamical properties of the system (ALLEN, 2004). MD is a "microscopic" approach based on the solving of the system's equations of

motion. This is fundamentally the Newton's second law ($\boldsymbol{F} = m\boldsymbol{a}$) for a classical system. The resultant force $\boldsymbol{F}$ has several sources in our case: the interaction potentials, U_{2b} and U_{3b}, and the confinement potential U_{conf}. Thus, for the i-th particle, MD intends to solve

$$m\frac{d\boldsymbol{v}_i}{dt} = \boldsymbol{F}_i = -\boldsymbol{\nabla}_i U$$

$$m\frac{d\boldsymbol{v}_i}{dt} = -\boldsymbol{\nabla}U_{conf}(r_i) - \sum_{j,k}^{N}[\,\boldsymbol{\nabla}U_{2b}(r_{ij}) + \boldsymbol{\nabla}U_{3b}(r_{ij}, r_{ik}, r_{jk})] \tag{3.9}$$

where $\boldsymbol{v}_i$ is the velocity vector and $\boldsymbol{\nabla}$ is the gradient, both corresponding to the i-th particle.

However, this picture is still incomplete. To consider the particle's thermal motion we make use of the Langevin equation. It consists in a small modification of Newton's second law by adding a frictional (viscous) force proportional to $\boldsymbol{v}$ and a stochastic term $\boldsymbol{\gamma}_i(T,t)$. In this case, the particle dynamics is defined by

$$m\frac{d\boldsymbol{v}_i}{dt} = -\eta\boldsymbol{v}_i + \boldsymbol{\gamma}_i(T,t) - \boldsymbol{\nabla}U_{conf}(r_i) - \sum_{j,k}^{N}[\,\boldsymbol{\nabla}U_{2b}(r_{ij}) + \boldsymbol{\nabla}U_{3b}(r_{ij}, r_{ik}, r_{jk})]\,, \tag{3.10}$$

where η is the damping coefficient and T is the temperature. As the thermal fluctuations are represented in the form of a stochastic term, it is required to be a Gaussian process with

$$\langle\boldsymbol{\gamma}_i(t)\rangle_\gamma = 0, \tag{3.11}$$

the brackets indicating an average with respect to all realizations of $\boldsymbol{\gamma}_i$ (i.e., with respect to the $\boldsymbol{\gamma}_i$ ensemble).

Also, for each particle, we desire the "kicks" offered by the $\boldsymbol{\gamma}_i(T,t)$ in the system to be uncorrelated in time and in different directions. Thus, considering Kardar (2007), the following identity is invoked

$$\langle\boldsymbol{\gamma}_{i,\alpha}(t), \boldsymbol{\gamma}_{j,\beta}(t')\rangle = \eta^2 D\delta_{i,j}\delta_{\alpha,\beta}\delta(t-t') = 2\eta k_B T\delta_{i,j}\delta_{\alpha,\beta}\,\delta(t-t'). \tag{3.12}$$

α, β are the cartesian components of the force vector, $\delta_{i,j}$ is the Kronecker delta, $\delta(t-t')$ is the Dirac's delta function and D is the diffusion coefficient. In the Langevin dynamics, the expression for D is given by the Einstein-Smoluchowski relation

$$D = \frac{2k_B T}{\eta}, \tag{3.13}$$

which connects microscopic properties of the particle diffusion with macroscopic quantities such as the viscosity (DAINTITH, 2008). The relation 3.12 is the autocorrelation function of $\boldsymbol{\gamma}_i(T,t)$. It is a manifestation of the fluctuation-dissipation theorem, which associates a dissipating energy process with a reverse one linked to thermal fluctuations (KUBO, 1966). The simplest example is when a Brownian particle is submitted to the impacts of the surrounding

molecules, which act as a random driving force and also establishes a frictional (viscous) force when the system is submitted to some external excitation. Eq. 3.10 brings these two extra contributions to our system.

We adopt a simplified version of the Langevin dynamics which is called Brownian dynamics (BD). BD can be considered an overdamped Langevin dynamics, in which the inertia term in Eq. 3.10 is small in comparison to the damping force (i.e., the acceleration is negligible). It means that Eq. 3.10 can be approximately written as

$$\eta \frac{d\boldsymbol{r}_i}{dt} \approx \boldsymbol{\gamma}_i(T,t) - \boldsymbol{\nabla} U_{conf}(r_i) - \sum_{j,k}^{N} [\, \boldsymbol{\nabla} U_{2b}(r_{ij}) + \boldsymbol{\nabla} U_{3b}(r_{ij}, r_{ik}, r_{jk})], \tag{3.14}$$

where the identity $\boldsymbol{v}_i = \dfrac{d\boldsymbol{r}_i}{dt}$ was used and $\boldsymbol{r}_i = (x_i, y_i)$.

3.3 NUMERICAL INTEGRATION

Our intention is to integrate Eq. 3.14 in order to obtain the position coordinates (x_i, y_i) of all particles at each time. Thus, we need to numerically integrate the Langevin equation. The procedure is described in Kardar (2007) and Tome and Oliveira (2014) through a finite difference method. This is a simple method which combines the Euler integration method for the deterministic component of the force (F) and uses a first-order approximation for the stochastic term. This is known as the Euler-Maruyama method. The x component of this approximation is given by

$$\eta[x_i(t_{n+1}) - x_i(t_n)] = F_{i,x}(t_n)\Delta t + \eta u_x(t_n)\sqrt{D\Delta t}$$

$$x_i(t_{n+1}) = x_i(t_n) + \frac{1}{\eta} F_{i,x}(t_n)\Delta t + u_x(t_n)\sqrt{D\Delta t} \tag{3.15}$$

where $F_{i,x}(t_n)$ is the x component of $-\boldsymbol{\nabla} U$ for the particle i, $u_x(t_n)$ is a Gaussian random variable (with zero mean and unit variance), $\Delta t = 0.001$ (in units of $\eta\, r_o^2/E_o$) is the time step and $\eta = 1.0$. An expression, similar to Eq. 3.15, is also assumed for y component and the two expressions are used to obtain particle positions with time.

3.4 SIMULATED ANNEALING AND OPTIMIZATIONS

We start the simulation by a random sorting of particles in a squared region, whose size is determined by a reference from $k_3 = 0$ case, which indicates a region of side $\sqrt{2N}$. This value guarantees a density of $\frac{2}{\pi}$ particles per area unit at $t = 0$.

A simulated annealing (SA) is used in our simulations in order to obtain our equilibrium arrangements and avoid metastable configurations. This procedure is based on the slowly

decrease of a high initial temperature (T) of the system in order to obtain a local minimum of the system at $T = 0$. The use of the SA is required to overcome the energy barrier between the close metastable states and get as closer as possible to the global minimum of the system for a given pair of N,k_3.

The initial temperature T_0 (in units of E_0/k_B, where k_B is the Boltzmann constant) is controlled by the parameter $D \propto T$ (Eq. 3.15). T_0 is such that the system is virtually a "liquid", when particles are accessing all the sorting region. In order to reach $T = 0$, we adopt a temperature reduction function which decays exponentially. A linear function was also tested, but adopted only for the case of a few particles. Starting with $k_B T = 8\,E_0$, we let the particles interact for $10^5\,\Delta t$. After that, there is a decrease in T by a factor of $\Delta T = 0.9$, along another time interval of $10^5\,\Delta t$. This is repeated for 80 temperature steps, until the reaching of a temperature value very close to $T = 0$, after which we set $T = 0$ and the equilibrium arrangement is finally obtained. Figure 20 shows the temperature function with the exponential decay.

Figure 20 – Temperature decrease curve in our simulated annealing. In the left, the full exponential decrease curve from $k_B T = 8.0\,E_0$ in $t = 0$. In the inset, last 40 steps in the temperature decrease with log scale in y axis.

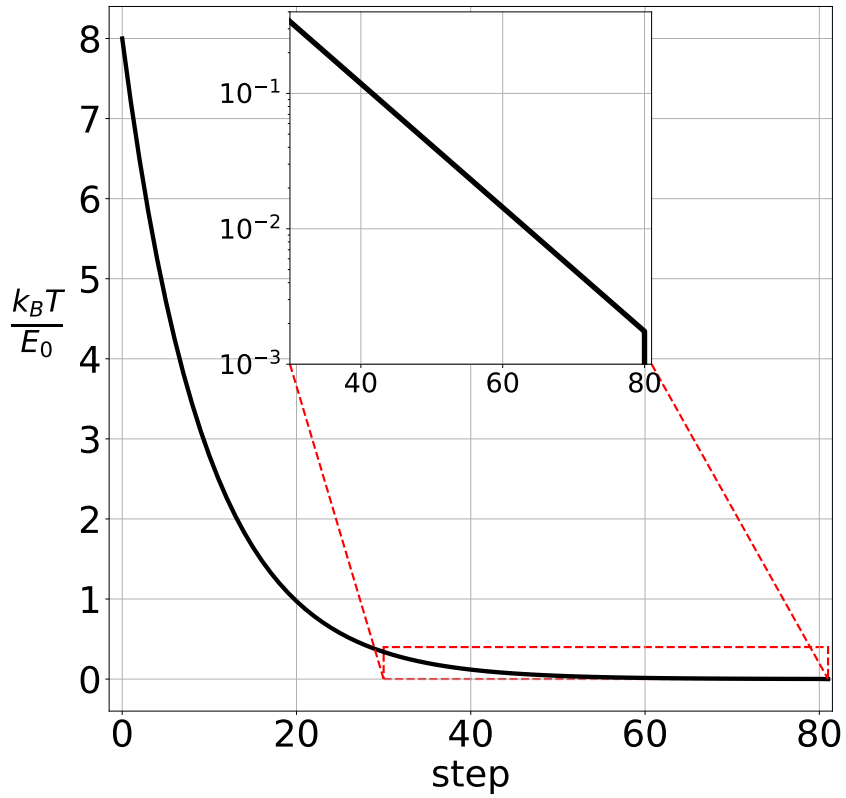

Source: The author (2021).

Due to the three-body interaction, code optimization is essential to save computational time. Besides the cutoff radius used to U_{3b} potentials, we make use of several strategies. One of these avoids extra iterations in the algorithm as we use Newton's third law in the (i, j)

particles loop through the identity

$$\boldsymbol{F}_{2b}(i;j) = -\boldsymbol{F}_{2b}(j;i) \tag{3.16}$$

where $\boldsymbol{F}_{2b}(i;j)$ is the two-body force (due to the j-th particle). In the case of the three-body potential $U_{3b} = U_{3b}(\boldsymbol{r}_i, \boldsymbol{r}_j, \boldsymbol{r}_k)$ we obtain an expression to simplify the three-body force calculations. Consider a trio of particles labeled by (i, j, k). The three-body force of the i-th particle due to the j-th and k-th particles is given by

$$\boldsymbol{F}_{3b}(i;j,k) = -\boldsymbol{\nabla}_i U_{3b} = -\frac{\partial U_{3b}}{\partial x_i}\hat{\boldsymbol{x}} - \frac{\partial U_{3b}}{\partial y_i}\hat{\boldsymbol{y}} \tag{3.17}$$

Working, for instance, with the x-component of Equation 3.17 and using the fact that $U_{3b} = U_{3b}(r_{ij}, r_{jk}, r_{ik})$, we apply the chain rule for partial derivatives

$$\begin{aligned} \boldsymbol{F}_{3b}(i;j,k)_x &= -\left(\frac{\partial x_{ij}}{\partial x_i}\frac{\partial U_{3b}}{\partial x_{ij}} + \frac{\partial x_{jk}}{\partial x_i}\frac{\partial U_{3b}}{\partial x_{jk}} + \frac{\partial x_{ik}}{\partial x_i}\frac{\partial U_{3b}}{\partial x_{ik}}\right) \\ &= -\left(\frac{\partial U_{3b}}{\partial x_{ij}} + \frac{\partial U_{3b}}{\partial x_{ik}}\right) \end{aligned} \tag{3.18}$$

Similarly for the three-body forces for the j- and k-th particles, we have the following relations

$$\begin{aligned} \boldsymbol{F}_{3b}(j;i,k)_x &= \frac{\partial U_{3b}}{\partial x_{ij}} - \frac{\partial U_{3b}}{\partial x_{jk}} \\ \boldsymbol{F}_{3b}(k;i,j)_x &= \frac{\partial U_{3b}}{\partial x_{ik}} + \frac{\partial U_{3b}}{\partial x_{jk}} \end{aligned} \tag{3.19}$$

Therefore, combining 3.18 and 3.19 we obtain

$$\boldsymbol{F}_{3b}(i;j,k)_x = -[\boldsymbol{F}_{3b}(j;i,k)_x + \boldsymbol{F}_{3b}(k;i,j)_x], \tag{3.20}$$

with a similar relation for the y-component. In this way, we can calculate only two of the three forces involved in a given particle trio. Equation 3.20 indicates that the sum of all three-body forces in the system is zero, which is similar to the two-body force case.

Also, we want to avoid, as much as we can, multiple calculations in the three-body interaction loop (the innermost loop in the algorithm), since it is computationally more expensive. Thus, we use lookup tables to storage *a priori* values of some function (exponentials, for example) in order to retrieve the value from the memory and not to perform the operation inside the loop (HALL; MCNAMEE, 1997).

4 TRAPPED PARTICLES: CONFINEMENT IN A PARABOLIC POTENTIAL

In this chapter, we present numerical and analytical results on the equibrium configuration of many particles confined to a parabolic potential U_{conf} (parabolic "trap") and interacting via two-body and three-body potentials. We will discuss the relevance of the three-body interaction to the system self-organization and the appearance of a first-order phase transition associated with a dramatic change in the particle density and in the system structure.

4.1 TWO-BODY INTERACTING PARTICLES REVISITED

We turn our attention to the confinement of particles in a parabolic potential with only the two-body interaction ($k_3 = 0$). This is a well-known system in the literature, so we can understand how the system arrangements are related to N and compare our simulation results with the available literature. In this situation, the particles were submitted to the repulsive U_{2b} (logarithmic, Coulomb-like or Yukawa-like) and the confinement potentials. Simulations were implemented for $3 \leq N \leq 50$ and some dozens of them were run per N, k_3. The energies were compared and the lowest energy arrangement was selected.

In order to avoid metastable states as much as possible, each simulation was carried out with the use of a simulated annealing to achieve the system equilibrium, as described in the Methodology chapter. We followed the procedure adopted in the Chapter 3, unless stated otherwise. As pointed out by Bedanov and Peeters (1994), as N increases, there are much more metastable configurations close to the global minimum, making it difficult to determine precisely the ground state. For this reason, we do not claim the obtained configurations are all ground states of the system, but the lowest energy metastable configurations we were able to find.

Now we describe our findings of this section. For all functional forms of U_{2b}, the equilibrium disposition was a single circular cluster of particles, organized in several concentric rings[1] composed of different number of particles. The equilibrium state is described by the label $(n_1, n_2, n_3, ...)$, where n_i designates the occupation number of the i-th shell. Essentially, the cluster is formed due to the combined presence of the aggregation offered by U_{conf} and the mutual particle repulsion caused by U_{2b} in the process of energy minimization. The repulsive interaction tries to form an hexagonal lattice in the infinite system, but the circularly symmetric harmonic confinement imposes the circular cluster formation (BEDANOV; PEETERS, 1994).

For a few particles ($N \leq 8$ for the Coulomb and Yukawa potentials and $N \leq 9$ for the logarithmic one), we observed the formation of regular polygons. For $6 \leq N \leq 9$, a central particle was found in the center of the polygon. Figure 21 shows such arrangements for k_2 and k_0 set to unity.

[1] In this work, a ring (or a shell) refers to two or more particles with the same radial position. A central particle is counted as a shell.

Figure 21 – Lowest energy arrangements for small values of N and $k_3 = 0.0$. From $N = 4$ to $N = 8$, the configurations were the same for all U_{2b} potentials. For Yukawa potential, $\lambda = 1.0$. Simulation boxes shown have dimensions of $1.7r_o \times 1.7\,r_o$. Dotted circles have unity radius, except for $N = 9$ (radius $1.5\,r_o$).

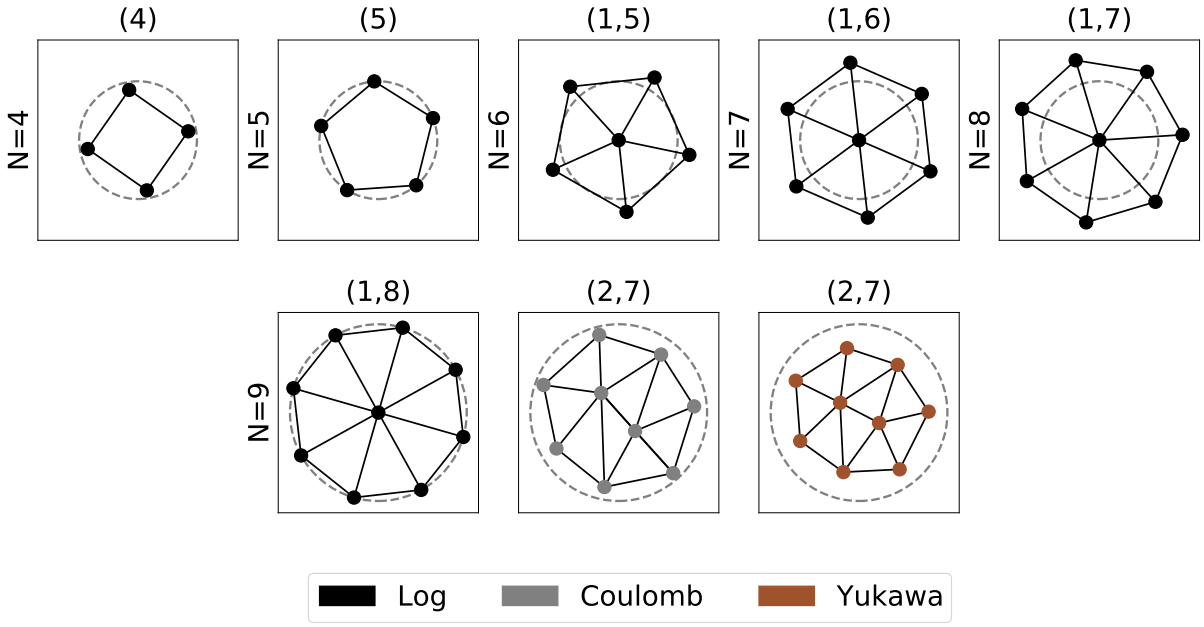

Source: The author (2020).

As we increase N, additional particles can populate the shells and, eventually, more rings are formed. Evidently, they also become more populated. Several cases are shown in Figure 22 also for k_2 and k_0 set to unity. The arrangements are very similar for all U_{2b} potentials, however there are small distinctions between them, with some fluctuations between the equilibrium states, which can be attributed to differences in the potential forms. Consider, for instance, the Yukawa potential. It has a shorter interaction range and a harder repulsive core (LAI; I, 1999), so the system "squeezes" a bit more than in the logarithmic case and a higher density is observed. Thus, we can observe deviations both in the arrangements size and in the ring occupation numbers, which is especially clear for $N = 46$. As already mentioned, adding particles to the system also implies more metastable states close to the global minimum, so the deviations in the ring occupation numbers should be more apparent for greater N.

As a consistency test for the simulation set in this section, we compared the results to some known references, such as Bedanov and Peeters (1994), Kong, Partoens and Peeters (2003) (based on Monte Carlo technique), Lai and I (1999) and Cheung, Choi and Hui (1997) (based on molecular dynamics simulation) for each U_{2b} potential.

A summary of the observed equilibrium configurations for $N > 9$ follows. Two rings were observed for $10 \leq N \leq 16$ (logarithmic) and for $10 \leq N \leq 15$ (Coulomb and Yukawa). Three rings for $17 \leq N \leq 33$ (logarithmic), $16 \leq N \leq 31$ (Coulomb) and $16 \leq N \leq 30$ (Yukawa). Four rings appeared for all remaining values until $N = 50$, except for an extra central particle for $N = 50$ in the Yukawa-like potential case. Except for only a few cases

Figure 22 – Lowest energy arrangements for several values of $10 \leq N \leq 50$ range and $k_3 = 0.0$. For Yukawa potential, $\lambda = 1.0$. Square boxes have the same sides in units of r_o for each N and shell numbers are indicated on the top of each.

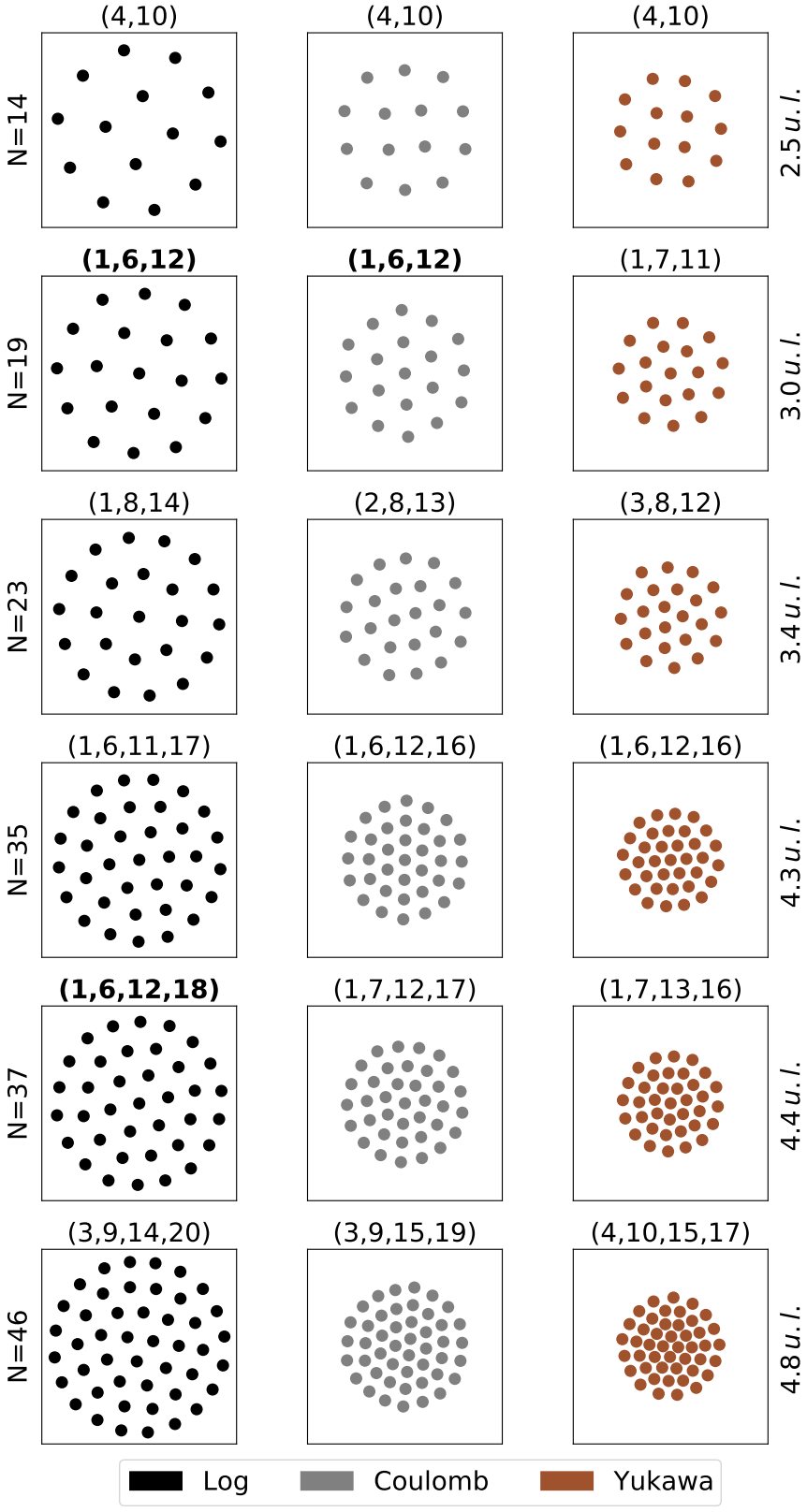

Source: The author (2020).

in which metastable energies were too close to each other, energy values and equilibrium arrangements were consistent with the references.

We also observed some "magic" configurations, for example the (1,6,12) at $N = 19$ for Coulomb and Yukawa and (1,6,12,18) at $N = 37$ for logarithmic potentials. They are marked in bold in Figure 22. According to works such as Bedanov and Peeters (1994) and Schweigert and Peeters (1995), these configurations are more stable than others against intershell rotation. The commensurability between different shells (the population of a shell being proportional to the population of another) and a high number of sixfold-coordinated particles (resembling an hexagonal lattice, except maybe for some defects in the boundary) are two special properties of these arrangements. In particular, for a uniform magic structure the difference between occupation number of these adjacent shells should be 6 (LAI; I, 1999).

As we use classical interactions in the Hamiltonian, in this work we approach the Thomson problem by studying "classical atoms". Similarly as Thomson, we can also summarize our results in a "classical" periodic table, which exhibits all the shell structures we found for the different U_{2b} in $3 \leq N \leq 50$ range. This is found in the Appendix A. An interesting feature is invoked by Lai and I (1999), which indicate that these "classical atoms" have different occupation number in the shells as N increases. We also observe this feature in our ring numbers for all U_{2b} potentials. In this context, the system allows new electrons to occupy also the inner shells, which is not the case in usual quantum atoms. This also occurs in three-dimensional classical systems, as registered in the shell configurations of Hasse and Avilov (1991), for example.

In the next section, we turn the three-body interaction on and focus on the influence of U_{3b} in the particle arrangements.

4.2 $k_3 \neq 0$: SYSTEM COMPACTION AND TRANSITIONS

4.2.1 $N = 3$: a prelude to the Gaussian three-body interaction

For $k_3 \neq 0$, we begin our investigation by the simplest possible case for the three-body interaction to appear, $N = 3$. In the following, we adopt k_2 and k_0 unitary. By means of a preliminary analytical study, Figure 23 gives us some hints on the energy behavior. We proceeded by fixing two particles in symmetrical positions with respect to the y-direction. It was followed by an evaluation of the potential energy $U(x, y)$ landscape for which a third particle would be submitted if placed in (x, y).

The Figure 23 shows the heat map for U, which is composed of

- a fixed parabolic confinement potential U_{conf};
- a fixed two-body repulsive logarithmic potential U_{2b} (the map is quite similar for the alternative functional forms); and

- a three-body attractive Gaussian potential U_{3b}, whose strength (k_3) is a variable parameter.

Figure 23 – Potential energy heat map as seen by a third particle, considering the logarithmic two-body interaction. We used $\xi_{3b} = r_o$ and the fixed particles positioned in (-0.3,0.0) and (0.3,0.0). The color bar indicates energy values in units of E_o and the square box has side of $1.0\,r_o$. The white crosses indicate local minima.

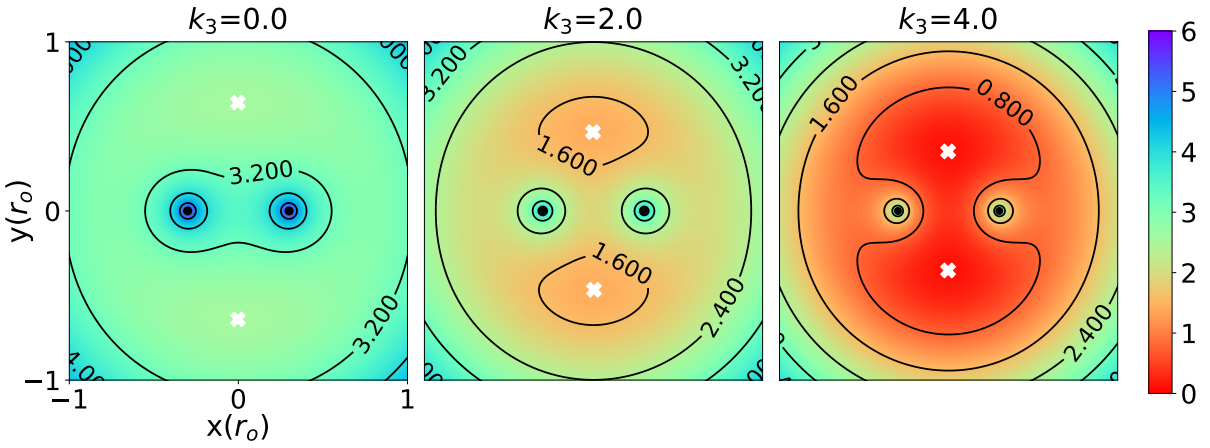

Source: The author (2021).

The case for $k_3 = 0.0$ (left, Fig.23) refers to the absence of the three-body interaction, in which U_{conf} is the only aggregating potential and the system experiences a larger repulsion region due to U_{2b} than in $k_3 \neq 0.0$ situation. As we increase the absolute value of k_3, an attractive potential (U_{3b}) comes in and a vertical region along the two fixed particles is promoted to lower energy. Red areas indicate regions with lower energies, so a third particle would prefer to occupy such locations if added to the system. The white crosses in Figure 23 (right) indicate the local minima of $U(x, y)$. The minima migrate to smaller radial positions as we increase k_3. That considered, a question on the system arrangement arises: if placed to freely interact with each other, what disposition would the three particles form after reach equilibrium? In what follows, we describe the semi-analytical study adopted in order to find it.

Considering Figure 23, an educated guess is that the particles can arrange themselves in the vertices of an equilateral triangle or even in a triplet, as shown in Figure 24. The distances between the particles can be simply described by functions of one parameter, L. Thus, for both configurations, we parameterized all the potentials (Eq. 3.8) by L. In this way, we obtain the potential energy of the system for each candidate configuration and check, through numerical simulations, which one is thermodynamically favourable. An analog of this procedure is used for several values of N in a following section.

This study is inspired by considerations in Sellin and Babaev (2013), which verify the influence of non-pairwise interactions in the ground state of three particles as the cause for structural changes in a given particle system. Depending on the ground state arrangement for $N = 3$, we predict the tendency of particles to arrange themselves into hexagonal symmetric structures (if a triangular ground state is the case) or into stripe-like configurations in systems

with many particles (if the triplet state is favourable). Thus, we want to check whether there is a change in the ground state caused by the introduction of the three-body interaction. Due to the small number of particles, we can fundamentally associate our configuration as a global minimum for $N = 3$.

Figure 24 – Proposed arrangements for particle positions for N=3, in the presence of a Gaussian three-body interaction. Left: equilateral triangle. Right: an equally distanced triplet.

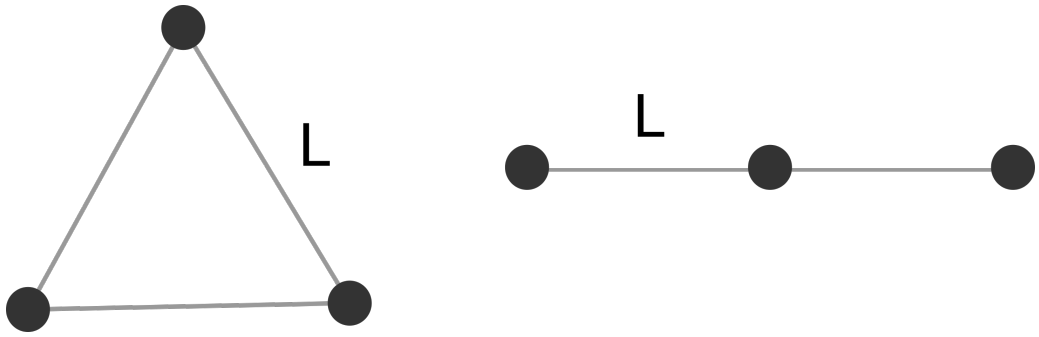

Source: The author (2020).

The expressions for the potential energy adopting the logarithmic two-body interaction are, then,

$$U_{eq.\,triangle} = L^2 - 3\log L - k_3 \exp\left(-\frac{3L^2}{2}\right) \tag{4.1}$$

and

$$U_{triplet} = 2L^2 - (2\log L + \log 2L) - k_3 \exp(-3L^2), \tag{4.2}$$

where U_{conf}, U_{2b} and U_{3b} are represented by each term in both equations, respectively.

Eqs. 4.1 and 4.2 are plotted in Figure 25A and 25B, respectively. In both cases, U_{conf} and U_{2b} are fixed. For the pair of solutions, the plotted curves for different k_3 indicate a deeper potential well in the region around the minima for greater k_3, which is associated with a system compaction. This is expected, as the attractive nature of the three-body interaction pull the particles close together. In particular, the triangular arrangement exhibited the smallest energy values.

We confirm such behavior by using the minimization process for U in an almost continuous range of k_3. The potential minima, obtained for specific values of L (L_{min}) at each k_3, are shown in Figure 25C. We observe that the three-body interaction favors the equilateral triangle disposition, for which corresponds the lowest energy values in all the range considered. A similar result is also found for Yukawa and Coulomb cases. The numerical simulations corroborate our analysis: only the triangle configuration was observed in the complete range of k_3 considered. Figure 25D displays the results and the expected compaction the system undergoes for greater k_3.

In the next section, we exhibit our findings for small values of N.

Figure 25 – In A and B, the parameterized potential energy U (considering a fixed two-body logarithmic interaction and $\xi_{3b} = \frac{1}{\sqrt{2}} r_o$) for the equilateral triangle and triplet cases, respectively. U minima are shown in C, according to the U_{3b} amplitude and indicate the equilateral triangle as the favoured arrangement. Correspondingly, simulation results are shown in D, where circles indicate particle positions.

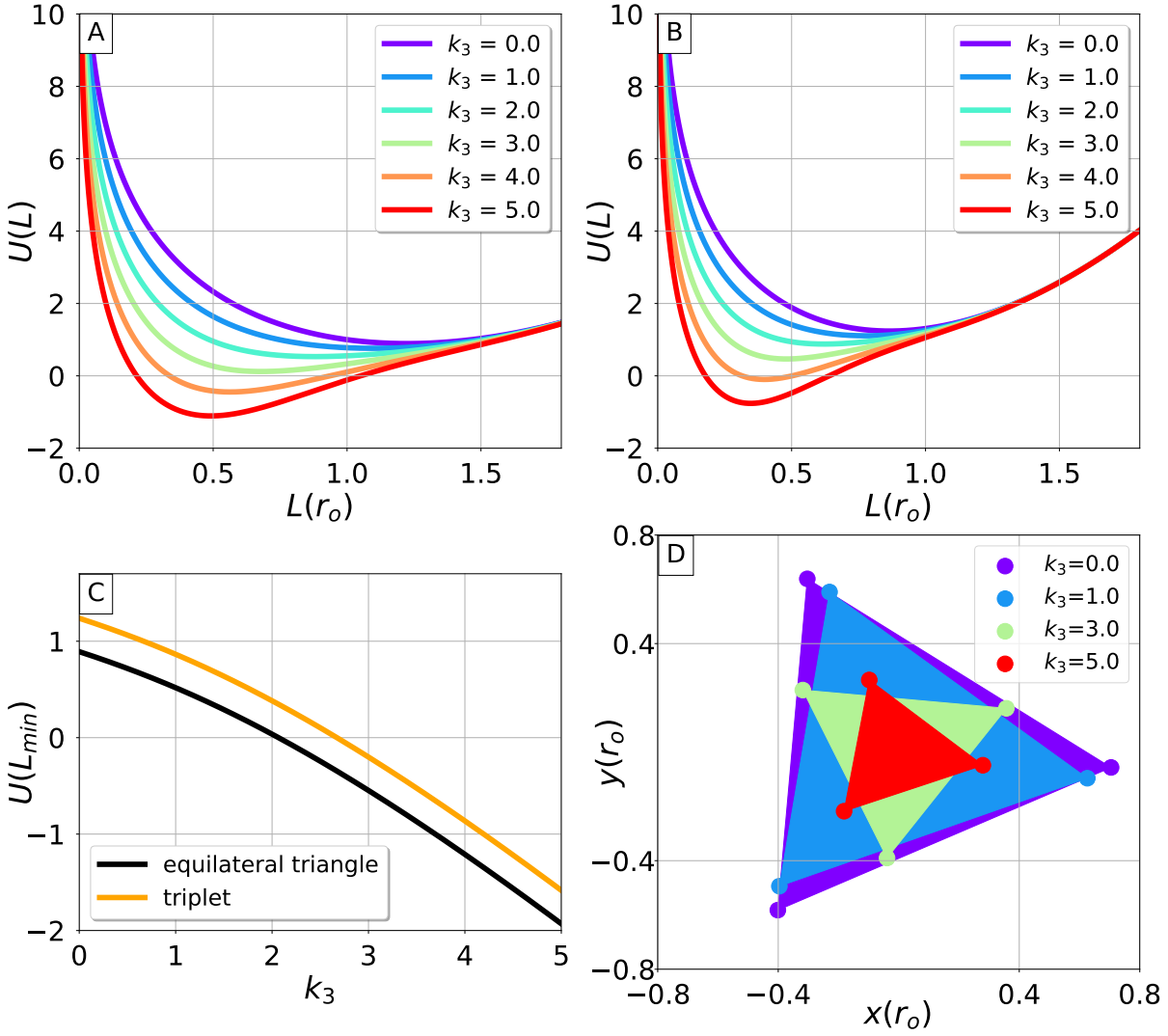

Source: The author (2020).

4.2.2 $N \leq 8$

For a small number of particles ($4 \leq N \leq 8$), we observed, through a semi-analytical study and MD simulations, that the introduction of a three-body interaction compacted the particle cluster in a similar way as we observed for $N = 3$, however with distinct behaviors for the different two-body potentials and with the existence of an special transition.

We conducted a semi-analytical study which adopts some equilibrium configuration ansätze for the system, such as

- $N = 4$: a square (4);

- $N = 5$: a square plus one central particle (1,4) or a pentagon (5);
- $N = 6$: a pentagon plus one central particle (1,5) or an hexagon (6);
- $N = 7$: an hexagon plus one central particle (1,6) or an heptagon (7); and
- $N = 8$: an heptagon plus one central particle (1,7) or an octagon (8).

Just as in Section 4.2, we compared this small set of configurations of $N = 5, 6, 7, 8$ to find which choice minimizes U. In the case of $N = 4$, no other configuration is found rather than the square one. We selected such polygon arrangements because we can parameterize U in terms of only one variable (the side of the polygon) and since we can expect that the polygonal structure found for $k_3 = 0$ and $N \leq 8$ will stand for $k_3 \neq 0$. This study is relevant because we compare it to our MD simulation results and it is useful because the expressions of U for $N \leq 8$ is still not cumbersome.

Figure 26 shows the energy profiles for small N after a numerical minimization of U. The solid curves shows the system local minima, without distinguishing the equilibrium configurations for each N. The effects of U_{3b} on these configurations will be discussed further below.

As we increase k_3, Coulomb and Yukawa cases show a smooth decrease in energy, which will be associated to a soft decrease in the polygon size. The behavior in the logarithmic potential is quite different, especially for $N = 6, 7, 8$, when we observe a sharp "knee" in the energy curve (grey dotted lines), indicating the presence of a sudden transition in the system. The region around this knee is associated with an abrupt contraction in the cluster size. Figure 26D confirms the existence of a discontinuous derivative of the energy plot for the logarithmic case. This discontinuity of $\frac{dU}{dk_3}$ resembles a first order phase transition in the system (KOCH, 1984), in which the first derivative of a function suffers a discontinuity in relation to some parameter. According to Figure 26D, the amplitude of such discontinuity is dependent on the number N of particles. Then, it is dependent on the three-body interaction strength as it grows when more particles are available to interact. It is important to consider that the Coulomb potential also exhibits such discontinuity, but only for greater N, as we shall see in the next section. Above $k_3 = 2.0$, for all cases of $N \leq 8$ the system continued to monotonically decrease in energy with no further discontinuities.

The appearance of a first-order transition in physical systems is associated with the phenomenon of bistability, i.e., the presence of two local minima (metastable equilibrium points) in the potential energy (KOCH, 1984). Figure 27 illustrates such phenomenon in our potential energy for two values of N. In what follows, we explain the motivation for this effect. For small values of k_3, the parabolic potential U_{conf} is the main responsible for the cluster cohesion: a single equilibrium point is assigned to the system, around $L = 1.2$ for $N = 7$ (Figure 27, left). However, considering the attractive nature of U_{3b}, as we increase its amplitude we reach a region where U_{3b} becomes relevant and two minima are defined in the system ($L \approx 0.5$ and

Figure 26 – Numerical study for the few-particles case. A, B and C show the energy dependence on k_3. We adopt $\xi = r_o$. D, E and F exhibit the energy derivatives with respect to k_3 indicating an abrupt transition in the logarithmic case. Triangles indicate energy results from MD simulation.

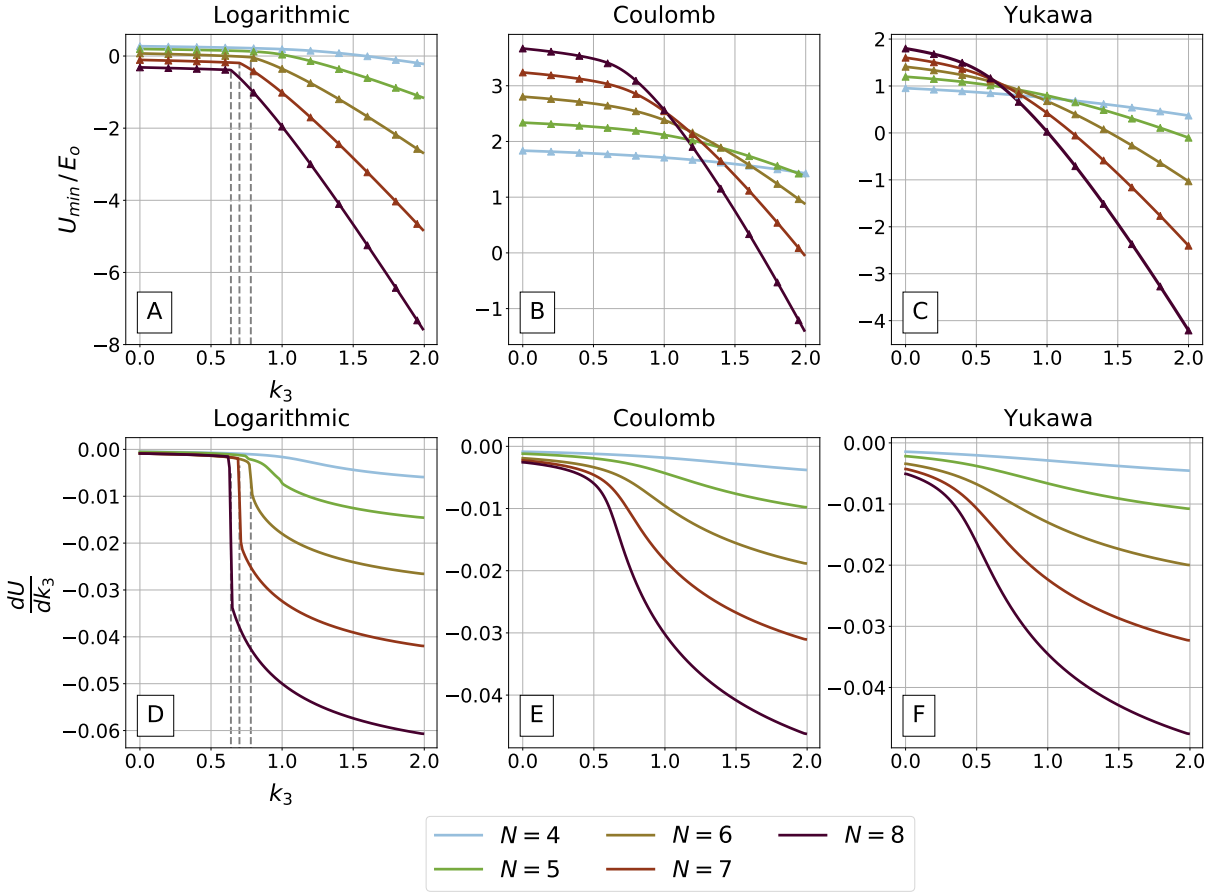

Source: The author (2020).

$L \approx 1.1$). Another increase in k_3 induces the dominance of U_{3b} over U_{conf} and the three-body interaction determines the cluster cohesion as the system (now smaller in size) reaches again a unique equilibrium point ($L \approx 0.5$). A similar situation occurs for $N = 8$ (Figure 27, right).

The importance of the transition region can be visualized with a simple study: turning off the parabolic confinement and observing the behavior of the particle configuration afterwards. Figure 28 shows the case for $N = 8$ and the logarithmic two-body potential. It can be seen that in the region of k_3 before the transition (for instance, $k_3 = 0.62$), the absence of the confinement prevents the system to hold the polygon structure together and the particles repel each other to the infinity, since the attractive three-body potential is still not strong. This is shown in the first row of Figure 28. However, when we choose a value of k_3 beyond the transition region ($k_3 = 0.74$), the confinement shutdown does not affect dramatically the configuration, only by a small displacement in particle positions. In this case, shown in the second row of Figure 28, only U_{2b} and U_{3b} potentials are fundamentally involved in the cluster cohesion, since U_{conf} is now negligible in comparison to U_{3b}.

We also observe the appearance of different metastable configurations for the same value of k_3 in the bistability region. Metastable states are found throughout the k_3 domain for different

Figure 27 – Bistability identified (dotted line) in the potential energy for $N = 7$ (left) around $k_3 = 0.72$ and $N = 8$ (right) around $k_3 = 0.64$. U_{2b} is the logarithmic potential and $\xi_{3b} = r_o$.

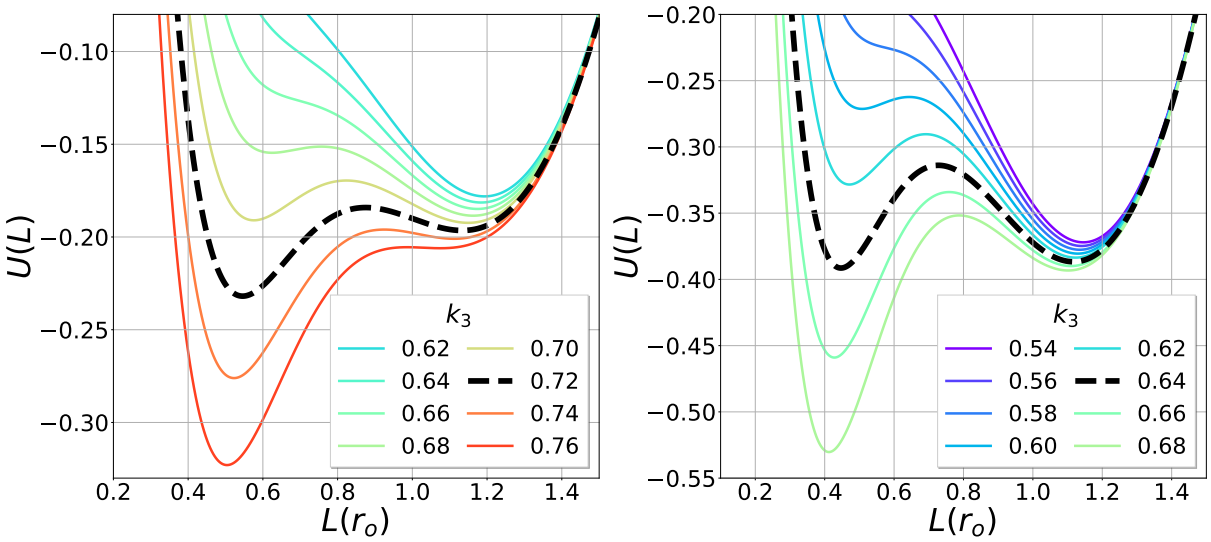

Source: The author (2020).

Figure 28 – Particle configuration after turning off the parabolic confinement at $t = 0$. U_{2b} is the logarithmic potential. In the first row, for $k_3 = 0.62$ (before the transition), the particle cluster loses the cohesion after $t > 0$ and the system is no longer stable. For $k_3 = 0.74$, the cluster remains stable for $t > 0$. In the latter case, only the competing interparticle potentials (U_{2b} and U_{3b}) ensure the cluster cohesion. Box sides are 1.6 and $5.2\, r_o$ in the first and second rows.

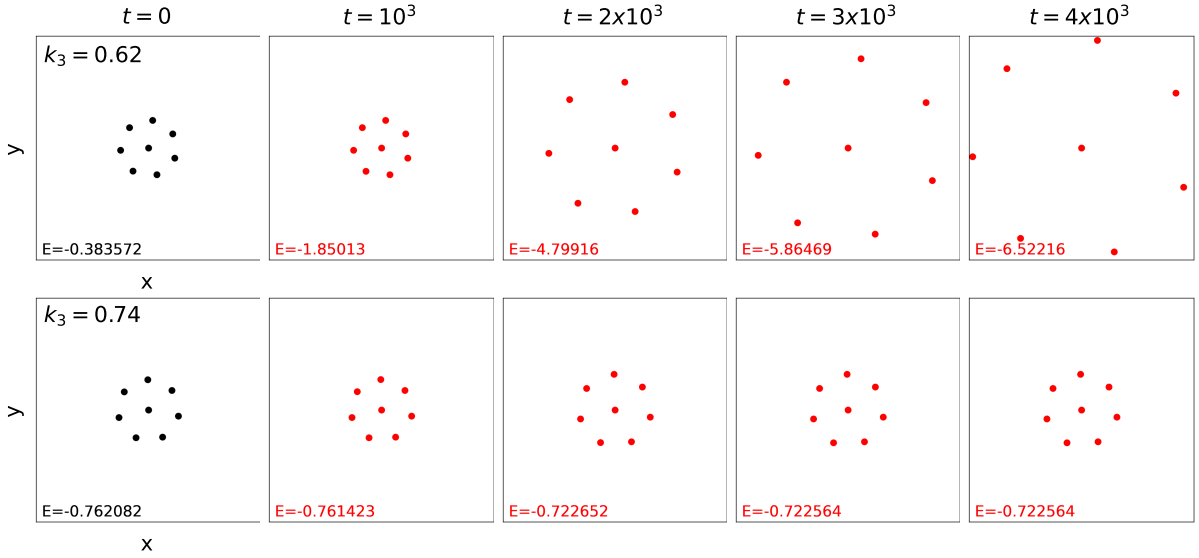

Source: The author (2021).

N and usually correspond to local minima very close with respect to size and energy. However, in the region of bistability, they can be associated to very different local minima (for instance, the two minima observed in Figure 27). Figure 29 shows examples for $N = 7$ and $N = 8$. The value of k_3 is such that bistability can be verified. In the first row, two configurations (both an hexagon with a central particle) are detected in the simulations with very different size and energy, which is associated to the two minima in different values of L (Figure 27, left). In the

case of $N = 8$, we also detect a third $(2, 6)$ configuration (metastable), which has an energy very close to the $(1, 7)$ arrangement in the middle (Figure 29, second row). For both rows of Figure 29, the configurations in the right are the equilibrium states.

Figure 29 – Different metastable configurations for the same value of k_3 in the region of the potential bistability. Cases are shown for $N = 7$ and $N = 8$ and the logarithmic two-body potential.

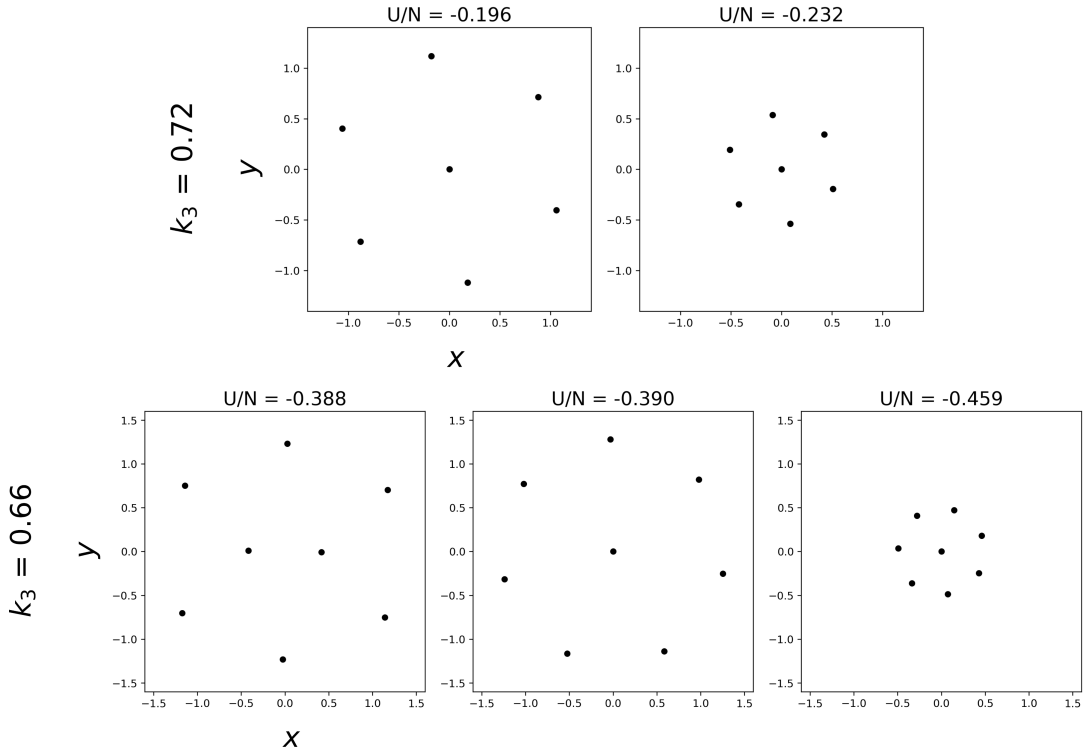

Source: The author (2021).

The introduction of U_{3b} make the system compacts as we increase k_3. Figure 30 shows an example of the system compaction for $N = 7$. Yukawa-like U_{2b} (Figure 30, first row) is associated with a smooth cluster contraction, while we confirm the existence of an abrupt compaction in the logarithmic case due to the transition around $k_{3,t} = 0.72$ (Figure 30, second row).

Another effect due to the three-body potential is observed. In general, our semi-analytical study showed an agreement with the $k_3 = 0$ case (listed in the Appendix A) in respect to the ring occupation numbers. However, in the parameter region around the energy discontinuity we detected some deviations in the shell numbers. With the further increase of k_3, after the discontinuity, the equilibrium configuration goes back to the arrangement listed in the Appendix A. Figure 31 exhibits the cases in which the ring numbers suffered such deviations, which are highlighted in red colors. With the use of the logarithmic two-body potential, for $0.76 \leq k_3 \leq 0.99$ and $N = 5$, the $(1, 4)$ configuration becomes more favourable than the pentagon (Fig. 31, first row) and around $k_3 = 0.67$ in $N = 8$ (not shown), the $(2, 6)$ configuration becomes more favourable than the $(1, 7)$. $(2, 6)$ is a configuration which we did not considered in our analytical study. As the energy difference between these states is too small, we cannot

Figure 30 – Different types of cluster compaction observed for Yukawa (smoothly) and logarithmic (abruptly) U_{2b} potential with the introduction of the three-body interaction. We adopt $\xi = r_o$.

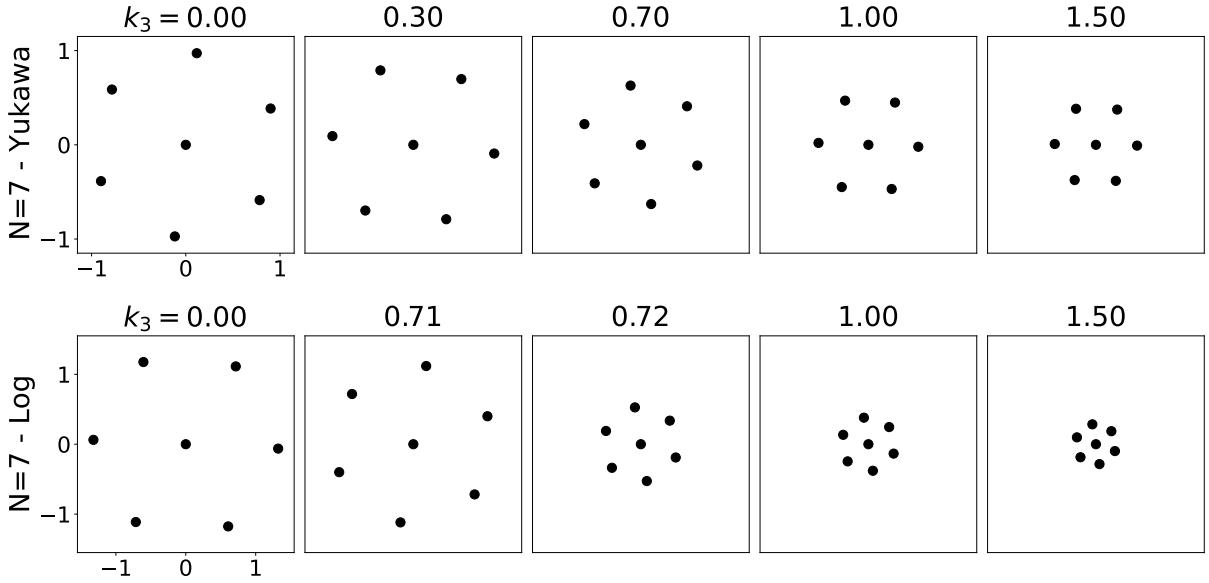

Source: The author (2020).

perceive any deviations between analytical and numerical energies in Figure 26 for $N = 8$. Also for Yukawa and Coulomb potentials (Fig. 31, second and third rows), $N = 8$ case showed a transition from $(2, 6)$ to $(1, 7)$ shell configuration, although in different k_3 ranges: $0.42 \leq k_3 \leq 0.58$ and $0.48 \leq k_3 \leq 0.87$, respectively. In all the cases, the density quickly grows around the energy discontinuity region, pushing particles to inner shells and changing the configurations found for $k_3 = 0$.

Essentially, the three-body interaction affected the cluster size (increasing density) and caused small disturbances in the shell structure when a few particles are interacting. If we consider there are not many trios of particles available for small values of N, the influence of U_{3b} is still limited and, then, we can not observe major disturbances in the structure. The three-body potential, however, introduced the bistability in the system, which is associated with some interesting effects for greater N. In the next section, we will discuss our findings when more particles are considered in the interaction.

4.2.3 $9 \leq N \leq 20$

Tables 1, 2 and 3 indicate how the configurations changed for $9 \leq N \leq 20$ as we introduced U_{3b} in the interaction potential. In Table 1, we do not observe many differences in the shell occupation numbers for the logarithmic potential, except for deviations observed for a few values of k_3 for $N = 9, 10, 12, 15, 16, 17$ and 20. The first-order like transition the system undergoes, which we detected around $0.60 \leq k_{3,t} \leq 0.66$, is even sharper in comparison with the few particles case ($4 \leq N \leq 8$). Bold text indicates the compacted clusters after the

Figure 31 – Deviations observed in the shell occupation numbers of some configurations. Red particles belong to a new arrangement compared to $U_{3b} = 0$ case.

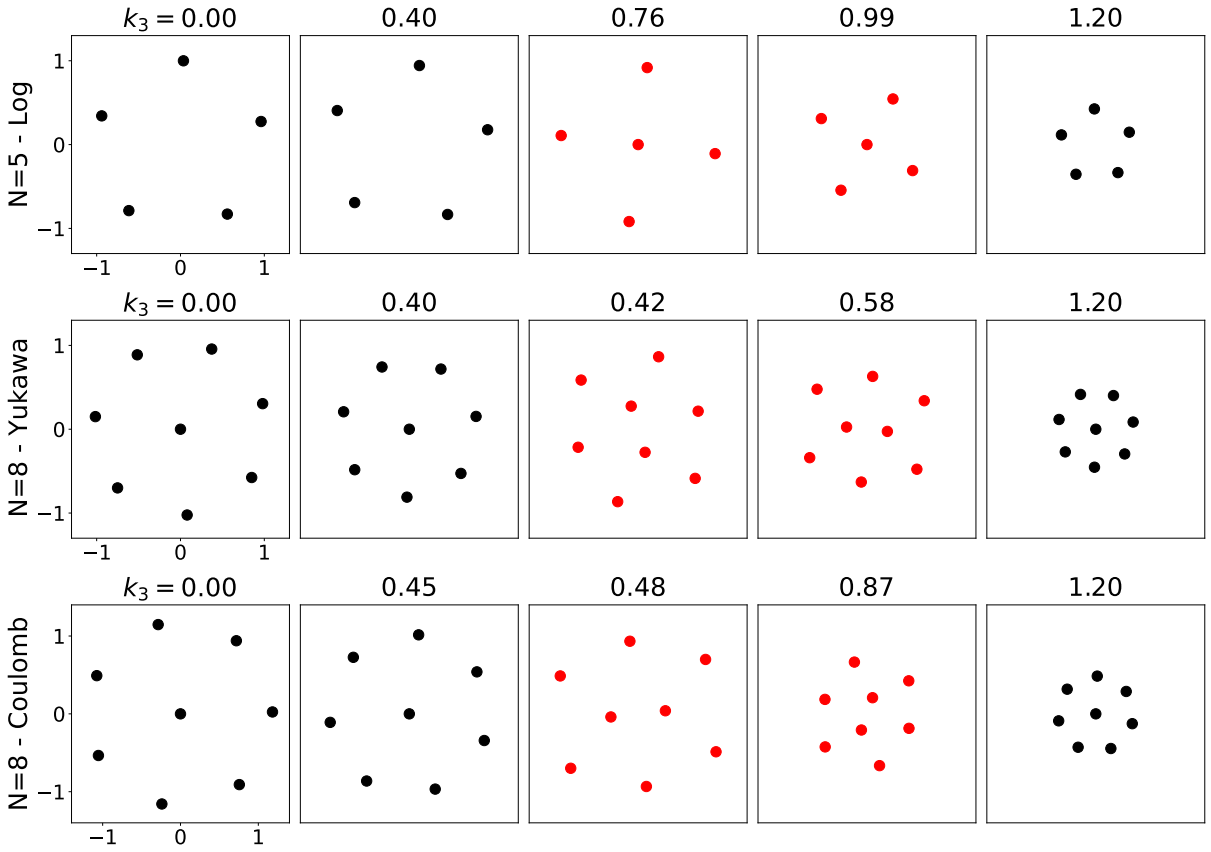

Source: The author (2020).

transition in Table 1. The transition from the initial cluster to these smaller arrangements is shown in Figure 32, which highlights the sudden compaction at $k_3 = k_{3,t} = 0.6$ for $N = 15$ and $N = 19$. Outside the transition vicinity, the system do not show great changes in size.

Tables 2 and 3 exhibit the equilibrium configurations for Coulomb and Yukawa potentials. The results indicate a well-defined distinction between logarithmic and Coulomb/Yukawa behavior with respect to the effect of the three-body interaction in the shell structure. As occurred in the Subsection 4.2.2, the cluster compaction around the transition is smoother, especially for Yukawa potential, and starts earlier than logarithmic case: $0.36 \leq k_{3,t} \leq 0.44$ for Coulomb and $0.24 \leq k_{3,t} \leq 0.36$ for Yukawa, considering $14 \leq N \leq 20$.

The cluster compaction in this case does not happen sharply as in the logarithmic case (see Figure 33, left), so we cannot estimate a standard transition point $k_{3,t}$ only by looking at the configurations. Hence, in the search for a standard point to represent the compaction, we select the point of maximum curvature (absolute value) in $U(k_3)$ curve: $|\frac{d^2U}{(dk_3)^2}|$, which has a peak in the middle region of the cluster compaction. This is shown by a dotted line in Figure 33, center and right. Looking at Tables 2 and 3 we can observe that particles arrange themselves in inner configurations specially in the transition region, according to the definition shown in the Figure 33. For example, the equilibrium configuration for $N = 20$ for the Yukawa

Figure 32 – Sudden cluster compaction identified at $k_3 = 0.6$ for $N = 15$ and $N = 19$ in the presence of the logarithmic U_{2b} potential. Simulation boxes have dimensions in r_o. For each row, the last two boxes have different scale.

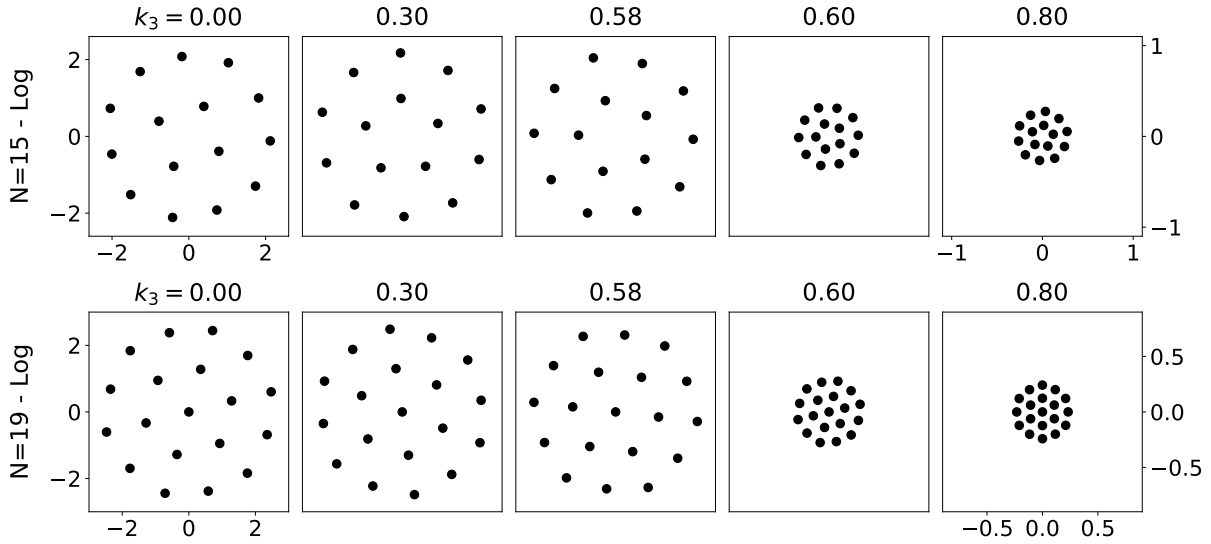

Source: The author (2020).

potential goes from $(1, 7, 12)$ at $k_3 = 0.0$, to $(2, 7, 11)$ at $k_3 = 0.12$ and, then, to $(2, 8, 10)$ at $k_3 = 0.2$, the latter occurring around the region of transition (Table 3).

Figure 33 – Energy (U/N) curves for specific N for all U_{2b} potentials. Center and right: energy and its first and second order derivatives plots to determine a standard point

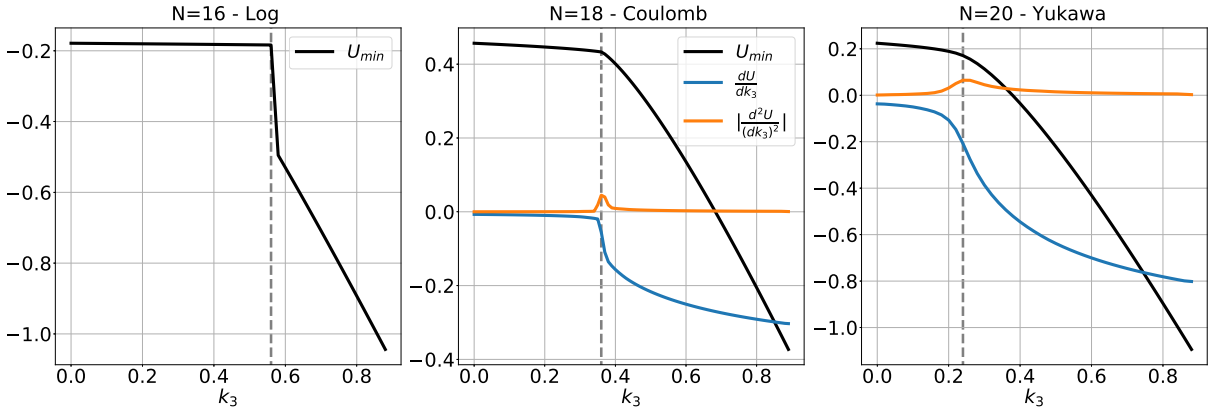

Source: The author (2021).

Figure 34 shows how the system evolves for increasing k_3 in the Coulomb and Yukawa cases. For these two forms of U_{2b}, compaction is accompanied by many changes in the shell occupation numbers. We verify the particle migration to inner shells, especially in the vicinity of the transition. These new arrangements, however, did not stand thermodynamically favorable for $k_3 >> k_{3,t}$, since we observe many of the preceding configurations becoming again the equilibrium states for $k_3 > 0.6$ (Tables 2 and 3).

Table 1 – Equilibrium configurations for $9 \leq N \leq 20$, logarithmic potential. Bold text indicates compacted cluster after the transition. Colors indicate different shell occupation numbers.

	k_3																	
N	**0.00**	**0.04**	**0.08**	**0.12**	**0.16**	**0.20**	**0.24**	**0.28**	**0.32**	**0.52**	**0.56**	**0.60**	**0.62**	**0.64**	**0.66**	**0.68**	**0.70**	**0.72**
9	1,8	1,8	1,8	1,8	1,8	1,8	1,8	2,7	2,7	2,7	2,7	2,7	2,7	2,7	**2,7**	**2,7**	**2,7**	**2,7**
10	2,8	2,8	2,8	2,8	2,8	2,8	2,8	2,8	2,8	2,8	3,7	3,7	3,7	**3,7**	**3,7**	**2,8**	**2,8**	**2,8**
11	3,8	3,8	3,8	3,8	3,8	3,8	3,8	3,8	3,8	3,8	3,8	3,8	3,8	**3,8**	**3,8**	**3,8**	**3,8**	**3,8**
12	3,9	3,9	3,9	3,9	3,9	3,9	3,9	3,9	3,9	3,9	3,9	3,9	4,8	**3,9**	**3,9**	**3,9**	**3,9**	**3,9**
13	4,9	4,9	4,9	4,9	4,9	4,9	4,9	4,9	4,9	4,9	4,9	4,9	**4,9**	**4,9**	**4,9**	**4,9**	**4,9**	**4,9**
14	4,10	4,10	4,10	4,10	4,10	4,10	4,10	4,10	4,10	4,10	4,10	**4,10**	**4,10**	**4,10**	**4,10**	**4,10**	**4,10**	**4,10**
15	4,11	4,11	5,10	5,10	5,10	5,10	5,10	5,10	5,10	5,10	5,10	**5,10**	**5,10**	**5,10**	**5,10**	**5,10**	**5,10**	**5,10**
16	5,11	5,11	5,11	5,11	5,11	5,11	5,11	5,11	5,11	5,11	5,11	**5,11**	**5,11**	**5,11**	**5,11**	**5,11**	**5,11**	**5,11**
17	1,5,11	1,5,11	1,5,11	1,5,11	1,5,11	1,5,11	1,5,11	1,5,11	1,5,11	1,5,11	1,5,11	**1,6,10**	**1,5,11**	**1,5,11**	**1,5,11**	**1,5,11**	**1,5,11**	**1,5,11**
18	1,6,11	1,6,11	1,6,11	1,6,11	1,6,11	1,6,11	1,6,11	1,6,11	1,6,11	1,6,11	1,6,11	**1,6,11**	**1,6,11**	**1,6,11**	**1,6,11**	**1,6,11**	**1,6,11**	**1,6,11**
19	1,6,12	1,6,12	1,6,12	1,6,12	1,6,12	1,6,12	1,6,12	1,6,12	1,6,12	1,6,12	1,6,12	**1,6,12**	**1,6,12**	**1,6,12**	**1,6,12**	**1,6,12**	**1,6,12**	**1,6,12**
20	1,6,13	1,7,12	1,7,12	1,7,12	1,7,12	1,7,12	1,7,12	1,7,12	1,7,12	1,7,12	1,7,12	**1,7,12**	**1,7,12**	**1,7,12**	**1,7,12**	**1,7,12**	**1,7,12**	**1,7,12**

Source: The author (2021).

Table 2 – Equilibrium configurations for $9 \leq N \leq 20$, Coulomb potential. Bold text indicate compacted cluster after the transition, according to the criteria exhibited in Figure 33. Colors indicates different shell occupation numbers.

	k_3																	
N	**0.00**	**0.04**	**0.16**	**0.20**	**0.28**	**0.32**	**0.34**	**0.36**	**0.38**	**0.40**	**0.42**	**0.44**	**0.46**	**0.48**	**0.52**	**0.56**	**0.68**	**0.72**
9	2,7	2,7	2,7	2,7	2,7	2,7	2,7	2,7	2,7	2,7	2,7	2,7	2,7	2,7	2,7	2,7	**2,7**	**2,7**
10	2,8	2,8	3,7	3,7	3,7	3,7	3,7	3,7	3,7	3,7	3,7	3,7	3,7	3,7	3,7	**3,7**	**3,7**	**3,7**
11	3,8	3,8	3,8	3,8	3,8	3,8	3,8	3,8	3,8	3,8	3,8	3,8	3,8	3,8	**3,8**	**3,8**	**3,8**	**3,8**
12	3,9	3,9	4,8	4,8	4,8	4,8	4,8	4,8	4,8	4,8	4,8	4,8	4,8	**4,8**	**4,8**	**4,8**	**4,8**	**4,8**
13	4,9	4,9	4,9	4,9	4,9	4,9	4,9	4,9	4,9	4,9	4,9	5,8	**5,8**	**4,9**	**4,9**	**4,9**	**4,9**	**4,9**
14	4,10	4,10	4,10	5,9	5,9	5,9	5,9	5,9	5,9	1,5,8	1,5,8	**1,5,8**	**5,9**	**5,9**	**5,9**	**5,9**	**5,9**	**5,9**
15	5,10	5,10	5,10	5,10	1,5,9	1,5,9	1,5,9	1,5,9	1,5,9	1,5,9	**1,5,9**	**1,5,9**	**1,5,9**	**1,5,9**	**1,5,9**	**1,5,9**	**1,5,9**	**5,10**
16	1,5,10	1,5,10	1,5,10	1,5,10	1,5,10	1,6,9	1,6,9	1,6,9	1,6,9	**1,6,9**	**1,6,9**	**1,6,9**	**1,6,9**	**1,6,9**	**1,5,10**	**1,5,10**	**1,5,10**	**1,5,10**
17	1,6,10	1,6,10	1,6,10	1,6,10	1,6,10	1,6,10	1,6,10	1,6,10	**1,6,10**	**1,6,10**	**1,6,10**	**1,6,10**	**1,6,10**	**1,6,10**	**1,6,10**	**1,6,10**	**1,6,10**	**1,6,10**
18	1,6,11	1,6,11	1,6,11	1,6,11	1,6,11	1,7,10	1,7,10	**1,7,10**	**1,7,10**	**1,7,10**	**1,7,10**	**1,6,11**	**1,6,11**	**1,6,11**	**1,6,11**	**1,6,11**	**1,6,11**	**1,6,11**
19	1,6,12	1,6,12	1,7,11	1,7,11	1,7,11	1,7,11	2,7,10	**2,7,10**	**1,7,11**	**1,7,11**	**1,7,11**	**1,7,11**	**1,7,11**	**1,7,11**	**1,7,11**	**1,7,11**	**1,7,11**	**1,7,11**
20	1,7,12	1,7,12	1,7,12	1,7,12	2,7,11	2,7,11	2,8,10	**2,7,11**	**2,7,11**	**2,7,11**	**2,7,11**	**2,7,11**	**2,7,11**	**2,7,11**	**2,7,11**	**1,7,12**	**1,7,12**	**1,7,12**

Source: The author (2021).

Table 3 – Equilibrium configurations for $9 \leq N \leq 20$, Yukawa potential. Bold text indicates compacted cluster after the transition, according to the criteria exhibited in Figure 33. Colors indicate different shell occupation numbers.

	k_3																	
N	**0.00**	**0.04**	**0.08**	**0.12**	**0.16**	**0.20**	**0.22**	**0.24**	**0.26**	**0.28**	**0.32**	**0.36**	**0.40**	**0.44**	**0.48**	**0.60**	**0.64**	**0.72**
9	2,7	2,7	2,7	2,7	2,7	2,7	2,7	2,7	2,7	2,7	2,7	2,7	2,7	2,7	2,7	**2,7**	**2,7**	**2,7**
10	2,8	3,7	3,7	3,7	3,7	3,7	3,7	3,7	3,7	3,7	3,7	3,7	3,7	**3,7**	**3,7**	**3,7**	**3,7**	**3,7**
11	3,8	3,8	3,8	3,8	3,8	3,8	3,8	3,8	3,8	3,8	3,8	3,8	**3,8**	**3,8**	**3,8**	**3,8**	**3,8**	**3,8**
12	3,9	4,8	4,8	4,8	4,8	4,8	4,8	4,8	4,8	4,8	4,8	4,8	**4,8**	**4,8**	**4,8**	**4,8**	**4,8**	**4,8**
13	4,9	4,9	4,9	4,9	4,9	4,9	4,9	4,9	4,9	4,9	4,9	**4,9**	**4,9**	**4,9**	**4,9**	**4,9**	**4,9**	**4,9**
14	4,10	4,10	5,9	5,9	5,9	5,9	5,9	5,9	5,9	5,9	5,9	**5,9**	**5,9**	**5,9**	**5,9**	**5,9**	**5,9**	**5,9**
15	5,10	5,10	5,10	5,10	1,5,9	1,5,9	1,5,9	1,5,9	1,5,9	1,5,9	**1,5,9**	**1,5,9**	**1,5,9**	**1,5,9**	**1,5,9**	**1,5,9**	**5,10**	**5,10**
16	1,5,10	1,5,10	1,5,10	1,5,10	1,5,10	1,6,9	1,6,9	1,6,9	1,6,9	1,6,9	**1,6,9**	**1,6,9**	**1,6,9**	**1,5,10**	**1,5,10**	**1,5,10**	**1,5,10**	**1,5,10**
17	1,6,10	1,6,10	1,6,10	1,6,10	1,6,10	1,6,10	1,6,10	1,6,10	1,6,10	**1,6,10**	**1,6,10**	**1,6,10**	**1,6,10**	**1,6,10**	**1,6,10**	**1,6,10**	**1,6,10**	**1,6,10**
18	1,6,11	1,6,11	1,6,11	1,6,11	1,6,11	1,7,10	1,7,10	1,7,10	1,7,10	**1,7,10**	**1,7,10**	**1,6,11**	**1,6,11**	**1,6,11**	**1,6,11**	**1,6,11**	**1,6,11**	**1,6,11**
19	1,7,11	1,7,11	1,7,11	1,7,11	1,7,11	1,7,11	2,7,10	2,7,10	**2,7,10**	**1,7,11**	**1,7,11**	**1,7,11**	**1,7,11**	**1,7,11**	**1,7,11**	**1,7,11**	**1,7,11**	**1,7,11**
20	1,7,12	1,7,12	1,7,12	2,7,11	2,7,11	2,8,10	2,8,10	**2,8,10**	**2,8,10**	**2,7,11**	**2,7,11**	**2,7,11**	**2,7,11**	**2,7,11**	**1,7,12**	**1,7,12**	**1,7,12**	**1,7,12**

Source: The author (2021).

Figure 34 – Equilibrium arrangements obtained with tunable three-body interaction for Coulomb and Yukawa potentials. Different background colors indicate different shell occupation numbers. Simulation boxes have dimensions in terms of r_o.

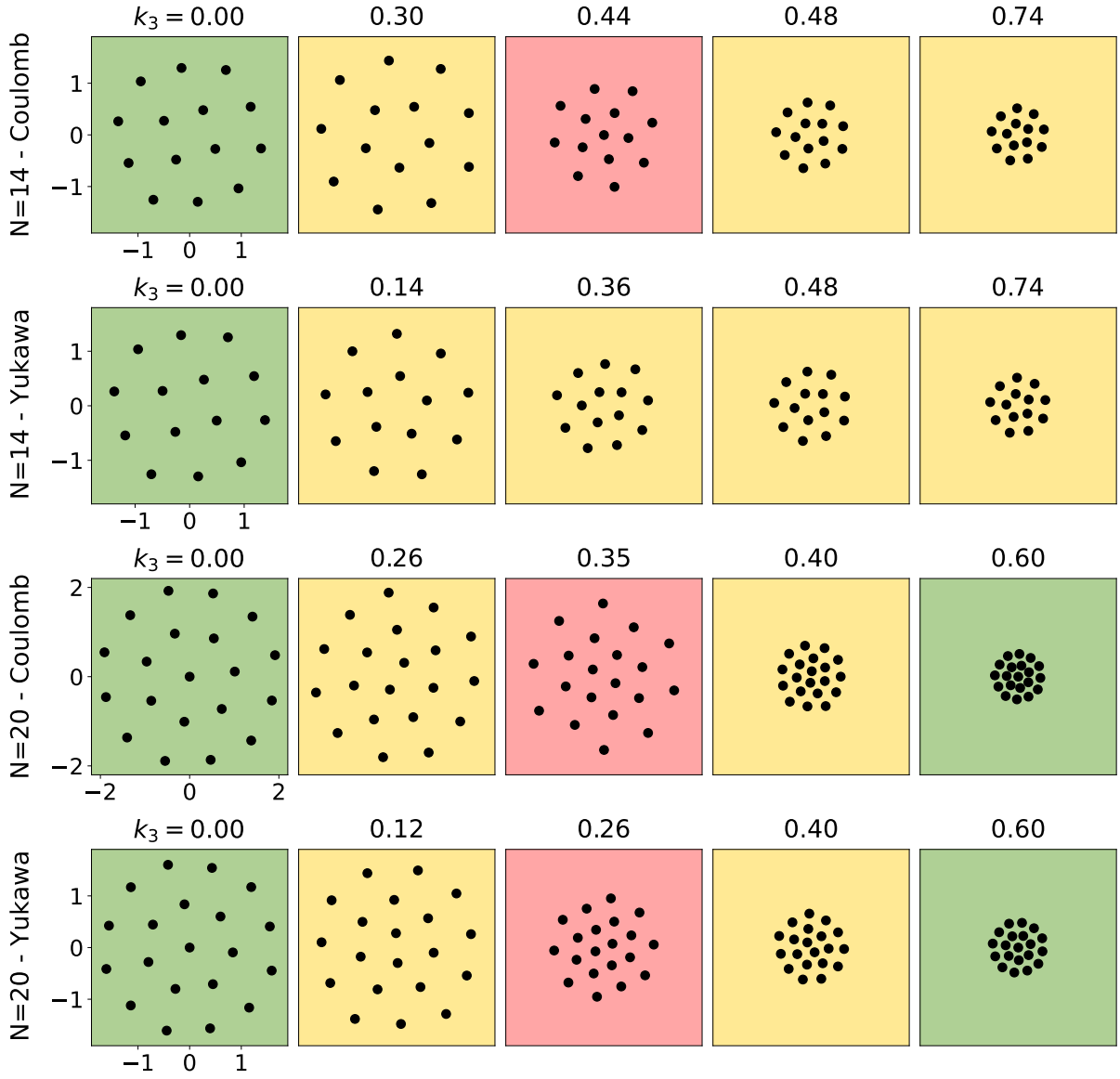

Source: The author (2021).

It is also possible to check how each metastable arrangement behaves with the introduction of the three-body potential for $9 \leq N \leq 20$. This requires a small modification in the simulation procedure. For a given N, we proceed by starting the simulation at some point of the k_3 range ($0.01 \leq k_3 \leq 0.8$) with the use of simulated annealing, obtaining an initial equilibrium arrangement for such point. Then, we vary k_3 in steps of 0.01, with no thermal noise. Our goal is to find the energy $E_{config.}(U/N)$ of such metastable states, understand how they behave in the transition and compare the results with the energies ($E_{ref.}$) found for the configurations of Tables 1, 2 and 3.

Figure 35 shows the energy difference $E_{config.} - E_{ref.}$ for Coulomb and Yukawa potentials. Note that a zero energy difference indicates the equilibrium configuration for a given k_3.

The plots suggest that around the transition ($k_3 = k_{3,t}$, grey dotted line) we observe the greatest changes in the shell occupation numbers, when some configurations are temporarily promoted to lower energy. Such arrangements contain more particles in the inner rings: for Coulomb potential and $N = 20$, $(1, 7, 12)$ goes to $(2, 7, 11)$ and $(2, 8, 10)$ around $k_3 = 0.3$, for example. After the transition, for $k_3 >> k_{3,t}$, the configurations goes back to the shell occupation numbers of $k_3 = 0$ case. When we vary k_3 with no thermal noise, the particles stay in positions slightly different than the local minima obtained in Tables 1, 2 and 3, so small oscillations above zero in the energy curve can be observed (Figure 35, $N = 20$, $k_3 \geq 0.6$, for example). This small study confirms that the transition is a special region in the system, where the inner configurations take place for $9 \leq N \leq 20$

Figure 35 – Energy difference between a given arrangement (obtained by the variation of k_3 in steps of 0.01 with $T = 0$), $E_{config.}$, and the equilibrium state obtained by the simulated annealing, $E_{ref.}$. Dotted grey lines show the cluster transition. Broken lines indicate not detected configurations for a given range of k_3.

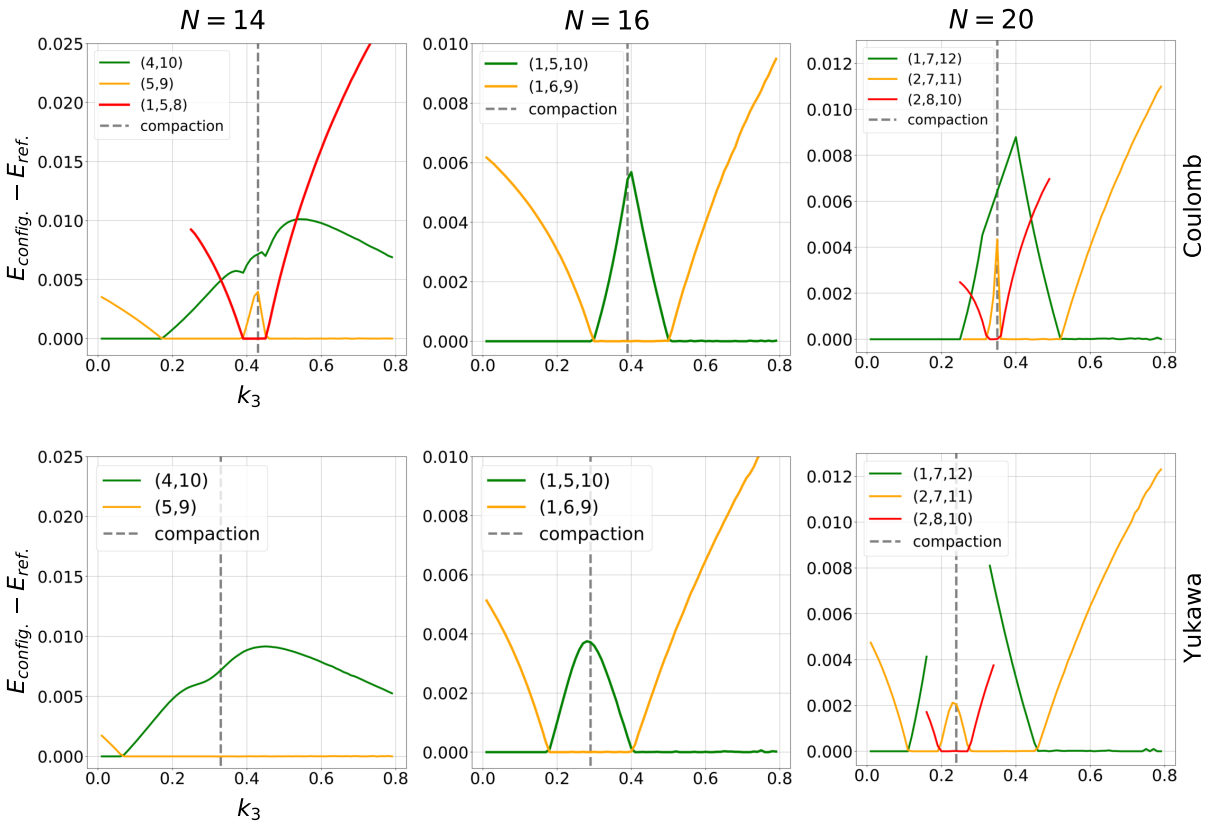

Source: The author (2021).

4.2.4 $21 \leq N \leq 50$

As we add more particles in the system, the Coulomb and Yukawa clusters continued to show changes in the shell numbers in comparison with their $U_{3b} = 0$ counterparts and the cluster compaction becomes sharper for both potentials and occurs for decreasing values of $k_{3,t}$. For these two potentials, we present simulation results up to $N = 50$ in Figure 36. We continue to observe the cluster compaction with no other structure arising. In this case, for $k_3 > 0.5$ and $N > 24$ the simulation did not converge numerically for $\Delta t = 0.001$. The reason for this incident may be associated with the typical time scale associated to both potentials in high-k_3 regime, since the particles self-assembly into a cluster very rapidly, implying a numerical imprecision. Changing our Δt by half or by a fourth allowed us to obtain results for $25 \leq N \leq 50$, however still incomplete for $k_3 > 0.5$ and $N > 40$. This is indicated in Figure 36 by the white region. To complete the diagram in our range of N and k_3, it would be necessary to use lower values of Δt or maybe change the method of integration.

Figure 36 – Equilibrium configurations for $21 \leq N \leq 50$, Coulomb and Yukawa potentials. White region indicates no data.

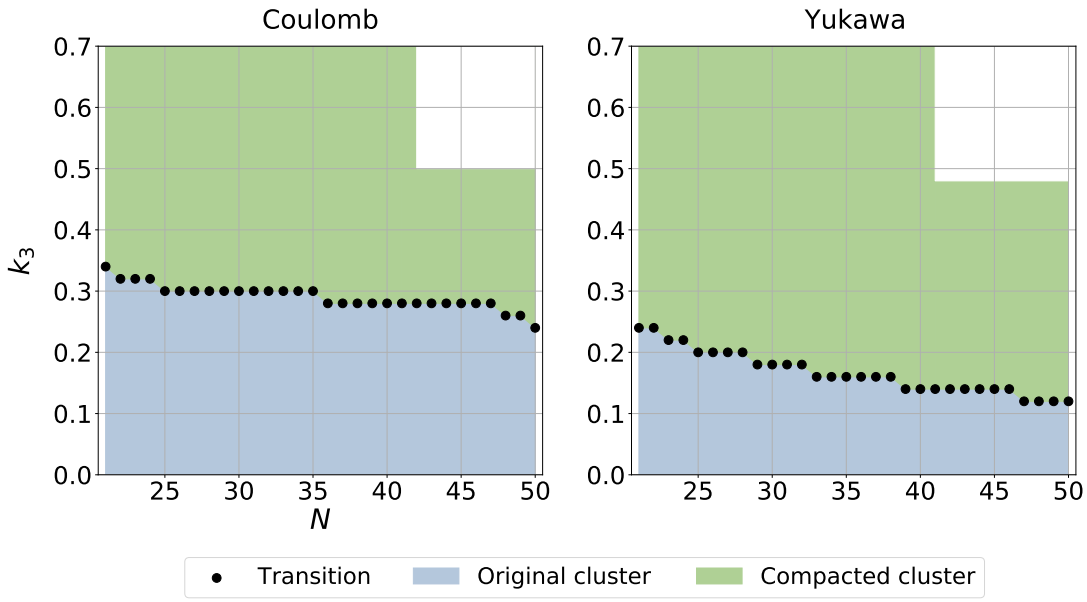

Source: The author (2021).

In the logarithmic potential case, we were able to obtain full results up to $N = 50$ and we observe a interesting effect. Until $N = 22$, we only notice the cluster compaction (Figure 37, first row) which accompanies the first-order transition. Starting from $N = 23$ at $k_{3\,(1+)} = 0.57$, this same transition is associated with the breaking of the initial cluster and the establishment of a new smaller cluster with some particles around it as the equilibrium state. An example of such configuration is shown in the second row of Figure 37, in which the $(2, 9, 14)$ cluster turns into a $(1, 7, 12)$ cluster and five surrounding particles ($k_{3\,(1+)} = 0.59$). From $N = 23$ to $N = 50$ this rearrangement occurred for $0.55 \leq k_{3\,(1+)} \leq 0.58$. Until $N = 38$ this was the only structural change observed as we increase k_3 in our range. These results are summarized

in the phase diagram of Figure 38, which is a product of around 100 annealing procedures for each N, k_3 pair.

For $N = 39$, a second change is observed at $k_{3\,(2+)} = 0.83$ (Figure 38), when two smaller clusters (plus surrounding particles) define the equilibrium arrangement. In the third row of Figure 37 we show this two-cluster configuration for $N = 40$. In this case, the initial $(1, 7, 14, 18)$ cluster changes into a smaller $(1, 6, 12)$ plus 21 particles forming a semicircular pattern at $k_{3\,(1+)} = 0.57$. Afterwards, at $k_{3\,(2+)} = 0.83$, two small clusters ($3, 9$ and $1, 7, 13$), plus 7 surrounding particles, are obtained. The fourth row shows a very similar situation for $N = 45$. This two-cluster configuration appears for smaller values of the U_{3b} amplitude as we increase N, reaching the minimum of $k_{3\,(2+)} = 0.68$ for $N = 50$.

The competition between U_{2b} and U_{3b} defines our results. The appearance of these smaller clusters reflects the high intensity of U_{3b}, which quickly pull near particles together during the system thermalization to form the smaller clusters, leaving some particles in the circular edge defined by U_{conf} (Figure 37, $N = 25$). The role of the U_{2b} long-range potential is to repel some surrounding particles outside the smaller cluster ($23 \leq N \leq 38$). Also due to U_{2b}, the two clusters repels each other for $39 \leq N \leq 50$, $k_3 \geq k_{3\,(2+)}$. A three-cluster formation is also observed in some of the annealing samples, however only as a metastable configuration. We expect it to appear as equilibrium arrangement for even greater values of N, as the two-cluster configurations appear firstly as metastable states for $k_3 < k_{3\,(2+)}$ and then, after $k_3 = k_{3\,(2+)}$, become the equilibrium state.

We note that the increase of N dramatically increases the number of metastable states with very close energies, once we have many distinct ways of arrange the particles with one or two clusters and the surrounding particles. This is confirmed by Figure 39, which shows a few energy profiles for $20 \leq N \leq 50$. We note that, as we increase the number of particles, we obtain a rougher energy landscape after the transition (Figure 39, second row). This is the outcome of many metastable states becoming accessible and energetically very close to each other. The results of Figure 38 are not at risk, since we detect energy deviations only with respect to similar configurations. In order to obtain a smoother energy curve, more samples in the annealing ensemble are required. This is expected because we verify that a small number of samples also produce a noisy energy curve for $N < 40$. However, increasing the number of annealing samples softens the curves.

Figure 37 – Some equilibrium configurations for $N > 21$ in the logarithmic U_{2b} potential situation. Respectively for each row, $N = 22$, $N = 25$, $N = 40$ and $N = 45$ are exhibited. $N = 25$ and $N = 40, 45$ cases show the breaking of the initial cluster into one or two smaller clusters, respectively. In the first row, three last columns are in different scale. Red squares show details of the smaller clusters.

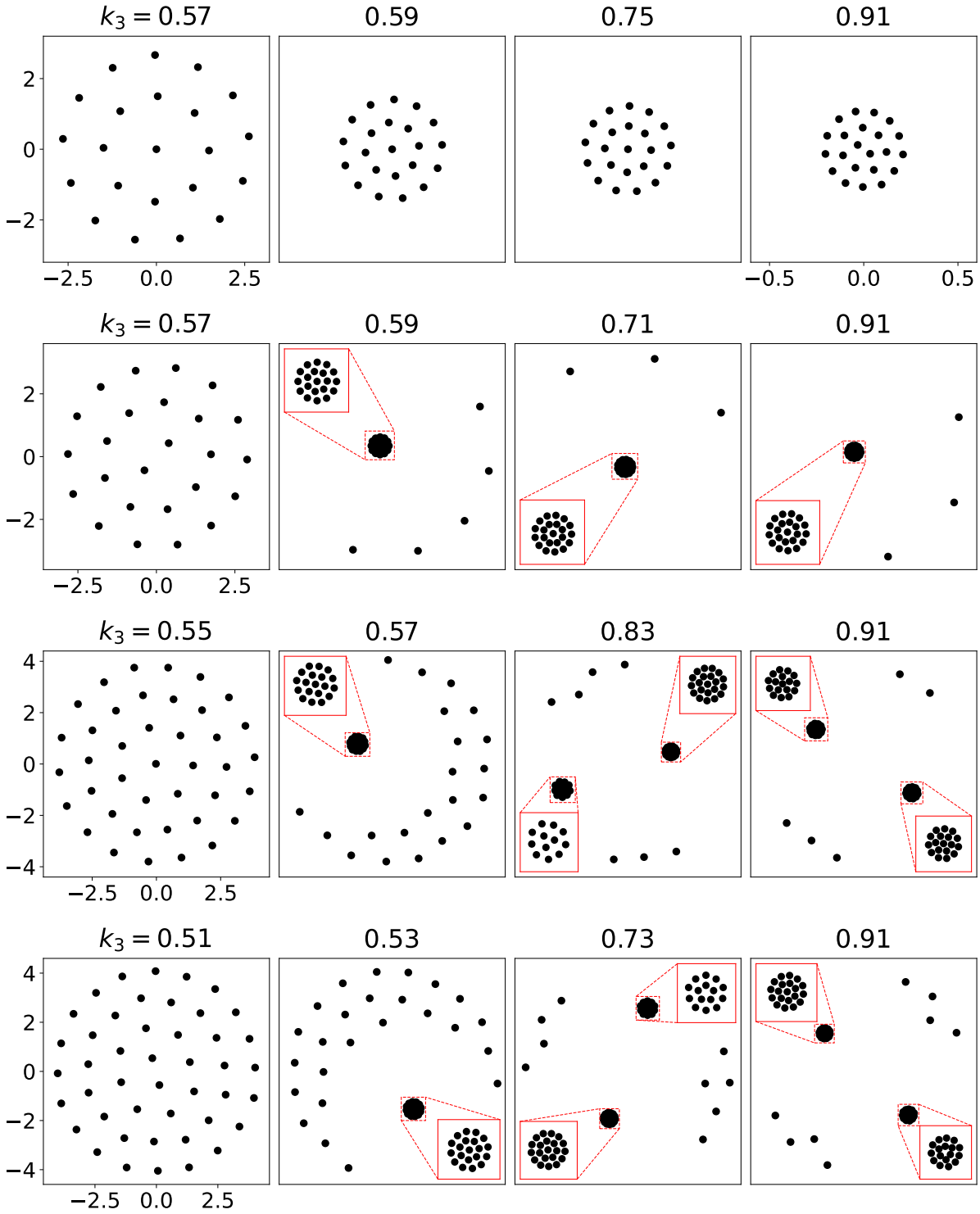

Source: The author (2021).

Figure 38 – Diagram of equilibrium states for the logarithmic potential and $9 \leq N \leq 50$.

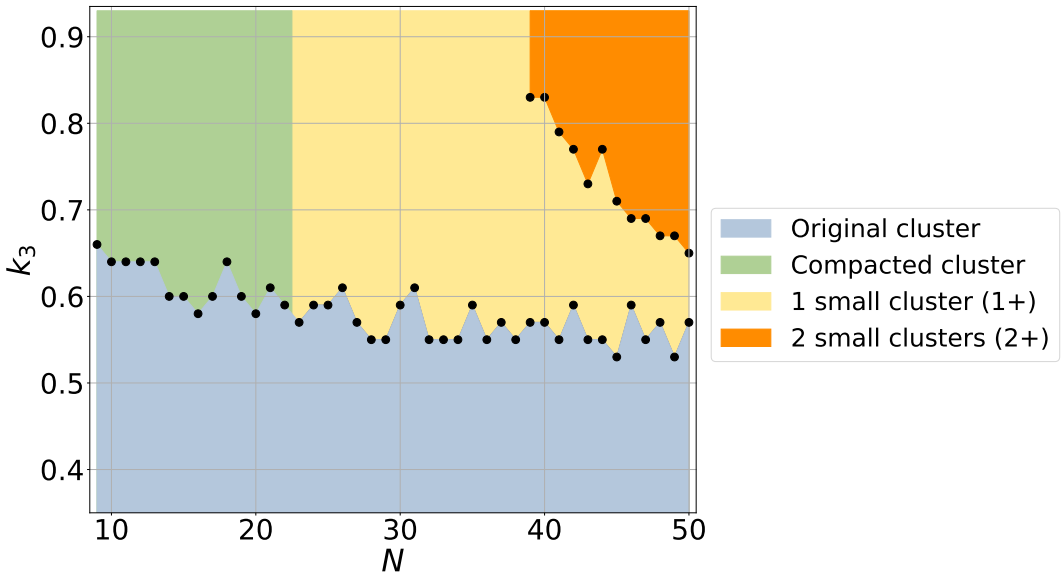

Source: The author (2021).

Figure 39 – Potential energy for some cases of $20 \leq N \leq 50$ for the logarithmic potential. Background colors indicate configuration according to Figure 38.

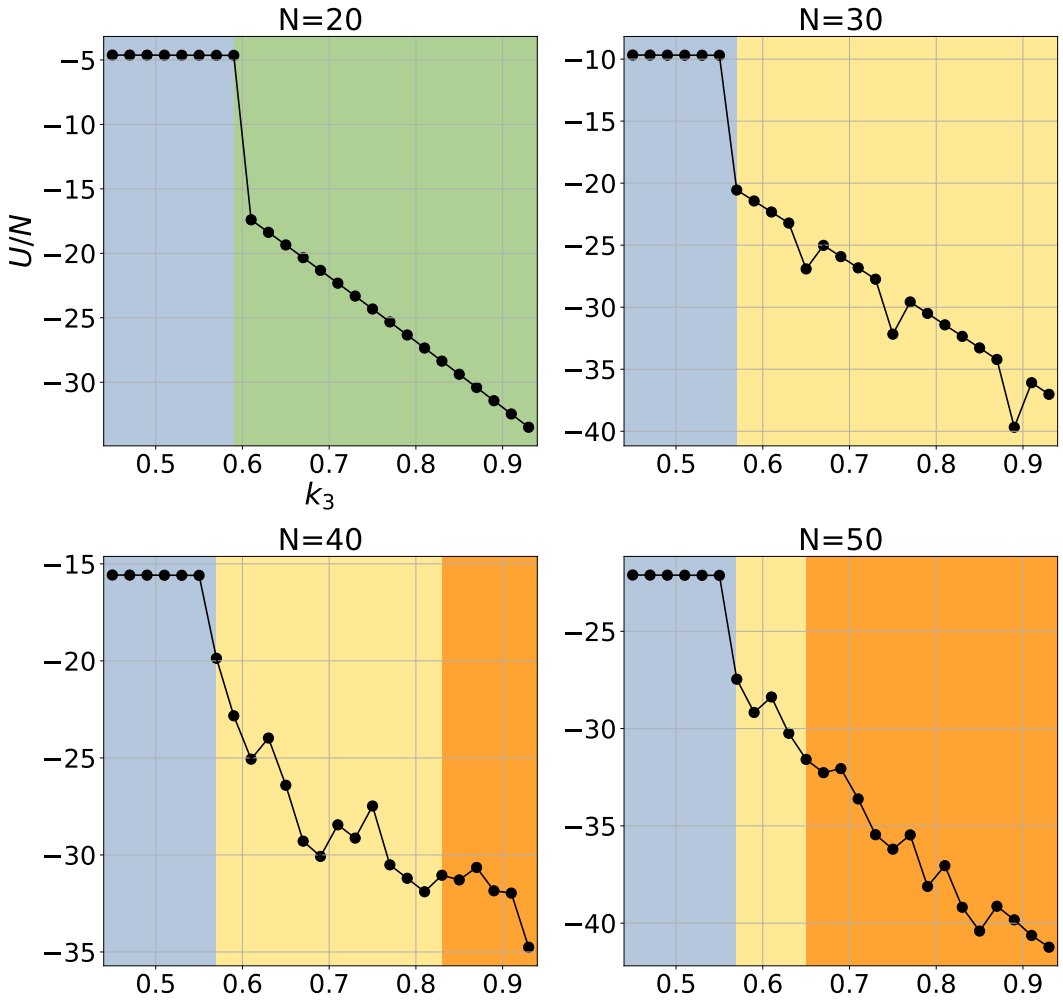

Source: The author (2021).

5 CONCLUSION

In this dissertation we studied the influence of the three-body interaction in the structure of two-dimensional particle clusters. Many numerical studies indicate structural changes in systems of superconductor vortices and important corrections in the charged colloids interaction due to three-body contributions. We investigated whether any structural change is detected for a system of $3 \leq N \leq 50$ particles confined by a parabolic potential when, besides the two-body purely repulsive potential, a three-body attractive potential is considered. We made use of Molecular Dynamics simulations and analytical calculations to obtain and compare stable and metastable particle configurations.

The results in the presence of typical repulsive two-body potentials only, when a structure of concentric shells is observed, were reproduced. When an attractive short-ranged three-body Gaussian potential is added, we also obtained the shell structure, however there were changes in the ring occupation numbers, even for $N < 20$. The main results include the emergence of a first-order transition associated with a cluster collapse into a smaller single cluster or into one or two smaller clusters with surrounding particles in a circular shape. These findings indicate the important role of the three-body interaction in the self-assembly of these particle clusters, since we obtain structural changes which resembles those obtained by two-body competing interactions, but only using monotonic two- and three-body competing potentials. A limitation of our work, which is possibly associated to the fast particle dynamics under a strong three-body potential, was the numerical imprecision of the simulation time step, which was not adequate to obtain convergence for Coulomb and Yukawa potentials for $N > 30$.

For future works, we expect to explore the influence of the Gaussian three-body interaction for a large number of confined particles ($N > 50$) and the influence of this and other functional forms of monotonic three-body potentials in the phase space of unconfined systems with periodic boundary conditions. The latter is motivated by rich phase diagrams recently obtained when one adopts competing two-body interactions.

REFERENCES

ALLEN, M. P. Introduction to molecular dynamics simulation. In: ATTIG, N.; BINDER, K.; GRUBM, H.; KREMER, K. (Ed.). *Computational Soft Matter: From Synthetic Polymers to Proteins*. [S.l.]: Mainz Max Planck Institute for Biophysical Chemistry and Gottingen Max Planck Institute for Polymer Research, 2004.

AXILROD, B. M.; TELLER, E. Interaction of the van der waals type between three atoms. *The Journal of Chemical Physics*, v. 11, n. 6, p. 299–300, 1943. Available at: <https://doi.org/10.1063/1.1723844>.

BEDANOV, V. M.; PEETERS, F. M. Ordering and phase transitions of charged particles in a classical finite two-dimensional system. *Phys. Rev. B*, American Physical Society, v. 49, p. 2667–2676, Jan 1994. Available at: <https://link.aps.org/doi/10.1103/PhysRevB.49.2667>.

BUCHLER, H. P.; MICHELI, A.; ZOLLER, P. Three-body interactions with cold polar molecules. *Nature Physics*, Springer Science and Business Media LLC, v. 3, n. 10, p. 726–731, Jul 2007. ISSN 1745-2481. Available at: <http://dx.doi.org/10.1038/nphys678>.

CÂNDIDO, L.; RINO, J. P.; STUDART, N.; PEETERS, F. M. The structure and spectrum of the anisotropically confined two-dimensional yukawa system. *Journal of Physics: Condensed Matter*, IOP Publishing, v. 10, n. 50, p. 11627–11644, dec 1998. Available at: <https://doi.org/10.1088/0953-8984/10/50/004>.

CARLSTRÖM, J.; GARAUD, J.; BABAEV, E. Semi-meissner state and nonpairwise intervortex interactions in type-1.5 superconductors. *Phys. Rev. B*, American Physical Society, v. 84, p. 134515, Oct 2011. Available at: <https://link.aps.org/doi/10.1103/PhysRevB.84.134515>.

CHEUNG, P.; CHOI, M.; HUI, P. Classical interacting particles in confinement. *Solid State Communications*, v. 103, n. 6, p. 357–360, 1997. ISSN 0038-1098. Available at: <https://www.sciencedirect.com/science/article/pii/S0038109897002007>.

DAINTITH, J. (Ed.). *Oxford Dictionary of Chemistry*. 6. ed. Oxford: Oxford University Press, 2008. ISBN 978–0–19–920463–2.

DHONT, J. K. G. *An introduction to dynamics of colloids*. [S.l.]: Elsevier, 1996. (Studies in interface science). ISBN 0-444-82009-4.

DOBNIKAR, J.; BRUNNER, M.; GRUENBERG, H. von; BECHINGER, C. Three-body interactions in colloidal systems. *Physical review. E, Statistical, nonlinear, and soft matter physics*, v. 69, p. 031402, 04 2004.

DOBNIKAR, J.; CHEN, Y.; RZEHAK, R.; GRüNBERG, H. H. von. Many-body interactions and the melting of colloidal crystals. *The Journal of Chemical Physics*, v. 119, n. 9, p. 4971–4985, 2003. Available at: <https://doi.org/10.1063/1.1595642>.

EDSTROM, A. *Non-pairwise vortex interactions in Ginzburg-Landau theory of superconductivity*. 64 p. Master's Thesis (Master's Thesis) — Royal Institute of Technology (KTH), 2012.

EDSTRÖM, A. Three and four-body intervortex forces in the ginzburg–landau models of single- and multicomponent superconductivity. *Physica C: Superconductivity*, v. 487, p.

19–26, 2013. ISSN 0921-4534. Available at: <https://www.sciencedirect.com/science/article/pii/S0921453413000233>.

FUJITA, J.-i.; MIYAZAWA, H. Pion Theory of Three-Body Forces. *Progress of Theoretical Physics*, v. 17, n. 3, p. 360–365, 03 1957. ISSN 0033-068X. Available at: <https://doi.org/10.1143/PTP.17.360>.

GLADILIN, V. N.; GE, J.; GUTIERREZ, J.; TIMMERMANS, M.; VONDEL, J. V. de; TEMPERE, J.; DEVREESE, J. T.; MOSHCHALKOV, V. V. Vortices in a wedge made of a type-i superconductor. *New Journal of Physics*, IOP Publishing, v. 17, n. 6, p. 063032, jun 2015. Available at: <https://doi.org/10.1088/1367-2630/17/6/063032>.

GUO, P.; GASPARIAN, V. Numerical approach for finite volume three-body interaction. *Phys. Rev. D*, American Physical Society, v. 97, p. 014504, Jan 2018. Available at: <https://link.aps.org/doi/10.1103/PhysRevD.97.014504>.

HALL, M.; MCNAMEE, J. P. *Improving Software Performance with Automatic Memoization*. 1997.

HAMAKER, H. The london—van der waals attraction between spherical particles. *Physica*, v. 4, n. 10, p. 1058–1072, 1937. ISSN 0031-8914. Available at: <https://www.sciencedirect.com/science/article/pii/S0031891437802037>.

HAMAKER, H. C. London-v. d. waals forces in colloidal systems. *Recueil des Travaux Chimiques des Pays-Bas*, v. 57, n. 1, p. 61–72, 1938. Available at: <https://onlinelibrary.wiley.com/doi/abs/10.1002/recl.19380570107>.

HAMMER, H.-W.; NOGGA, A.; SCHWENK, A. Colloquium: Three-body forces: From cold atoms to nuclei. *Rev. Mod. Phys.*, American Physical Society, v. 85, p. 197–217, Jan 2013. Available at: <https://link.aps.org/doi/10.1103/RevModPhys.85.197>.

HASSE, R. W.; AVILOV, V. V. Structure and madelung energy of spherical coulomb crystals. *Phys. Rev. A*, American Physical Society, v. 44, p. 4506–4515, Oct 1991. Available at: <https://link.aps.org/doi/10.1103/PhysRevA.44.4506>.

HESS, H. F.; ROBINSON, R. B.; DYNES, R. C.; VALLES, J. M.; WASZCZAK, J. V. Scanning-tunneling-microscope observation of the abrikosov flux lattice and the density of states near and inside a fluxoid. *Phys. Rev. Lett.*, American Physical Society, v. 62, p. 214–216, Jan 1989. Available at: <https://link.aps.org/doi/10.1103/PhysRevLett.62.214>.

IACOVELLA, C. R.; ROGERS, R. E.; GLOTZER, S. C.; SOLOMON, M. J. Pair interaction potentials of colloids by extrapolation of confocal microscopy measurements of collective suspension structure. *The Journal of Chemical Physics*, v. 133, n. 16, p. 164903, 2010. Available at: <https://doi.org/10.1063/1.3498746>.

JEAN, M. S.; EVEN, C.; GUTHMANN, C. Macroscopic 2d wigner islands. *Europhysics Letters (EPL)*, IOP Publishing, v. 55, n. 1, p. 45–51, jul 2001. Available at: <https://doi.org/10.1209/epl/i2001-00379-x>.

KARDAR, M. *Statistical Physics of Fields*. Cambridge, UK: Cambridge University Press, 2007.

KITTEL, C. *Introduction to Solid State Physics*. 7. ed. New York: John Wiley and Sons, 1996. ISBN 0-471-11181-3.

KOCH, S. W. *Dynamics of First-Order Phase Transitions in Equilibrium and Nonequilibrium Systems*. 1. ed. [S.l.]: Springer-Verlag Berlin Heidelberg, 1984. ISBN 978-3-540-13379-7.

KONG, M.; PARTOENS, B.; PEETERS, F. M. Structural, dynamical and melting properties of two-dimensional clusters of complex plasmas. *New Journal of Physics*, IOP Publishing, v. 5, p. 23–23, mar 2003. Available at: <https://doi.org/10.1088/1367-2630/5/1/323>.

KRAMER, L. Thermodynamic behavior of type-ii superconductors with small κ near the lower critical field. *Phys. Rev. B*, American Physical Society, v. 3, p. 3821–3825, Jun 1971. Available at: <https://link.aps.org/doi/10.1103/PhysRevB.3.3821>.

KUBO, R. The fluctuation-dissipation theorem. *Reports on Progress in Physics*, IOP Publishing, v. 29, n. 1, p. 255–284, jan 1966. Available at: <https://doi.org/10.1088/0034-4885/29/1/306>.

LAI, Y.-J.; I, L. Packings and defects of strongly coupled two-dimensional coulomb clusters: Numerical simulation. *Phys. Rev. E*, American Physical Society, v. 60, p. 4743–4753, Oct 1999. Available at: <https://link.aps.org/doi/10.1103/PhysRevE.60.4743>.

LING, X. S.; PARK, S. R.; MCCLAIN, B. A.; CHOI, S. M.; DENDER, D. C.; LYNN, J. W. Superheating and supercooling of vortex matter in a nb single crystal: Direct evidence for a phase transition at the peak effect from neutron diffraction. *Phys. Rev. Lett.*, American Physical Society, v. 86, p. 712–715, Jan 2001. Available at: <https://link.aps.org/doi/10.1103/PhysRevLett.86.712>.

LIU, Y. H.; CHEW, L. Y.; YU, M. Y. Self-assembly of complex structures in a two-dimensional system with competing interaction forces. *Phys. Rev. E*, American Physical Society, v. 78, p. 066405, Dec 2008. Available at: <https://link.aps.org/doi/10.1103/PhysRevE.78.066405>.

LOUIS, A. A. Beware of density dependent pair potentials. *Journal of Physics: Condensed Matter*, IOP Publishing, v. 14, n. 40, p. 9187–9206, Sep 2002. ISSN 0953-8984. Available at: <http://dx.doi.org/10.1088/0953-8984/14/40/311>.

MORBIDELLI, M.; AROSIO, P. *Polymer Reaction and Colloid Engineering. Lecture notes.* [S.l.]: Institute for Chemical and Bioengineering, ETH Zurich, 2016.

MOSHCHALKOV, V.; MENGHINI, M.; NISHIO, T.; CHEN, Q. H.; SILHANEK, A. V.; DAO, V. H.; CHIBOTARU, L. F.; ZHIGADLO, N. D.; KARPINSKI, J. Type-1.5 superconductivity. *Phys. Rev. Lett.*, American Physical Society, v. 102, p. 117001, Mar 2009. Available at: <https://link.aps.org/doi/10.1103/PhysRevLett.102.117001>.

PARTOENS, B.; PEETERS, F. M. Classical artificial two-dimensional atoms: the thomson model. *Journal of Physics: Condensed Matter*, IOP Publishing, v. 9, n. 25, p. 5383–5393, jun 1997. Available at: <https://doi.org/10.1088/0953-8984/9/25/007>.

PIEPER, S. C.; WIRINGA, R. B. Quantum monte carlo calculations of light nuclei. *Annual Review of Nuclear and Particle Science*, v. 51, n. 1, p. 53–90, 2001. Available at: <https://doi.org/10.1146/annurev.nucl.51.101701.132506>.

PRIMAKOFF, H.; HOLSTEIN, T. Many-body interactions in atomic and nuclear systems. *Phys. Rev.*, American Physical Society, v. 55, p. 1218–1234, Jun 1939. Available at: <https://link.aps.org/doi/10.1103/PhysRev.55.1218>.

REICHHARDT, C.; BISHOP, A. Structural transitions, melting, and intermediate phases for stripe and clump forming systems. *Physical review. E, Statistical, nonlinear, and soft matter physics*, v. 82, p. 041502, 10 2010.

SCHWEIGERT, V. A.; PEETERS, F. m. c. M. Spectral properties of classical two-dimensional clusters. *Phys. Rev. B*, American Physical Society, v. 51, p. 7700–7713, Mar 1995. Available at: <https://link.aps.org/doi/10.1103/PhysRevB.51.7700>.

SELLIN, K. A. H.; BABAEV, E. Stripe, gossamer, and glassy phases in systems with strong nonpairwise interactions. *Phys. Rev. E*, American Physical Society, v. 88, p. 042305, Oct 2013. Available at: <https://link.aps.org/doi/10.1103/PhysRevE.88.042305>.

SILVA, C. Clemente de S. *Propriedades de equilíbrio e de transporte da matéria de vórtices em nanoestruturas supercondutoras*. Phd Thesis (PhD Thesis) — Universidade Federal de Pernambuco, Departamento de Física, Pós-Graduação em Física, Recife, 2003.

THOMSON, J. J. On the structure of the atom: an investigation of the stability and periods of oscillation of a number of corpuscles arranged at equal intervals around the circumference of a circle; with application of the results to the theory of atomic structure. *The London, Edinburgh, and Dublin Philosophical Magazine and Journal of Science*, Taylor and Francis, v. 7, n. 39, p. 237–265, 1904. Available at: <https://doi.org/10.1080/14786440409463107>.

TINKHAM, M. *Introduction to Superconductivity: Second Edition*. [S.l.]: McGraw-Hill, 1996.

TOME, T.; OLIVEIRA, M. J. d. *Dinâmica Estocástica e Irreversibilidade*. São Paulo, SP: Editora Edusp, 2014. ISBN 9788531414800.

TREFALT, G.; BORKOVEC, M. *Overview of DLVO Theory*. [S.l.]: University of Geneva, 2014.

VERWEY, E. J. W. *Theory of the Stability of Lyophobic Colloids*. [S.l.]: Dover Publications, 1999. ISBN 978-0486409290.

XU, X. B.; TANG, T.; WANG, Z. H.; XU, X. N.; FANG, G. Y.; GU, M. Nonequilibrium pattern formation in circularly confined two-dimensional systems with competing interactions. *Phys. Rev. E*, American Physical Society, v. 103, p. 012604, Jan 2021. Available at: <https://link.aps.org/doi/10.1103/PhysRevE.103.012604>.

APPENDIX A – EQUILIBRIUM CONFIGURATIONS FOR $k_3 = 0$

	Logarithmic		Coulomb		Yukawa	
N	**shells**	U/N	**shells**	U/N	**shells**	U/N
3	*3*	0.297	*3*	1.310	*3*	0.700
4	*4*	0.273	*4*	1.836	*4*	0.953
5	*5*	0.195	*5*	2.339	*5*	1.197
6	*1,5*	0.073	*1,5*	2.805	*1,5*	1.410
7	*1,6*	-0.107	*1,6*	3.239	*1,6*	1.603
8	*1,7*	-0.314	*1,7*	3.669	*1,7*	1.799
9	*1,8*	-0.546	*2,7*	4.088	*2,7*	1.987
10	*2,8*	-0.810	*2,8*	4.485	*2,8*	2.161
11	*3,8*	-1.099	*3,8*	4.865	*3,8*	2.320
12	*3,9*	-1.415	*3,9*	5.239	*3,9*	2.480
13	*4,9*	-1.747	*4,9*	5.601	*4,9*	2.630
14	*4,10*	-2.102	*4,10*	5.959	*4,10*	2.781
15	*4,11*	-2.471	*5,10*	6.308	*5,10*	2.924
16	*5,11*	-2.857	*1,5,10*	6.650	*1,5,10*	3.063
17	*1,5,11*	-3.260	*1,6,10*	6.983	*1,6,10*	3.196
18	*1,6,11*	-3.678	*1,6,11*	7.308	*1,6,11*	3.326
19	*1,6,12*	-4.111	*1,6,12*	7.632	*1,7,11*	3.457
20	*1,6,13*	-4.555	*1,7,12*	7.950	*1,7,12*	3.583
21	*1,7,13*	-5.013	*1,7,13*	8.266	*2,7,12*	3.710
22	*1,7,14*	-5.480	*2,8,12*	1.981	*2,8,12*	3.830
23	*1,8,14*	-5.959	*2,8,13*	8.879	*3,8,12*	3.948
24	*2,8,14*	-6.451	*3,8,13*	9.176	*3,8,13*	4.062
25	*3,8,14*	-6.952	*3,9,13*	9.471	*3,9,13*	4.175
26	*3,9,14*	-7.464	*3,9,14*	9.763	*4,9,13*	4.287
27	*3,9,15*	-7.986	*4,9,14*	10.051	*4,9,14*	4.396
28	*4,9,15*	-8.515	*4,10,14*	10.336	*4,10,14*	4.504
29	*4,10,15*	-9.056	*4,10,15*	10.618	*5,10,14*	4.611
30	*4,10,16*	-9.603	*5,10,15*	10.897	*5,10,15*	4.717
31	*4,10,17*	-10.159	*5,11,15*	11.174	*1,6,10,14*	4.820
32	*4,11,17*	-10.722	*1,5,11,15*	11.447	*1,6,11,14*	4.920
33	*5,11,17*	-11.295	*1,6,11,15*	11.716	*1,6,11,15*	5.018
34	*1,5,11,17*	-11.874	*1,6,12,15*	11.983	*1,6,12,15*	5.116
35	*1,6,11,17*	-12.462	*1,6,12,16*	12.247	*1,6,12,16*	5.213

36	*1,6,12,17*	-13.057	*1,6,12,17*	12.511	*1,7,12,16*	5.310
37	*1,6,12,18*	-13.658	*1,7,12,17*	12.772	*1,7,13,16*	5.406
38	*1,6,12,19*	-14.266	*1,7,13,17*	13.030	*2,8,13,15*	5.501
39	*1,7,13,18*	-14.880	*2,8,12,17*	13.288	*2,8,13,16*	5.593
40	*1,7,13,19*	-15.501	*2,8,13,17*	13.542	*2,8,14,16*	5.685
41	*1,7,13,20*	-16.128	*2,8,14,17*	13.794	*3,8,14,16*	5.775
42	*1,7,14,20*	-16.760	*3,8,14,17*	14.044	*3,9,14,16*	5.864
43	*2,8,14,19*	-17.399	*3,9,14,17*	14.291	*3,9,14,17*	5.952
44	*2,8,14,20*	-18.045	*3,9,14,18*	14.538	*3,9,15,17*	6.040
45	*3,8,14,20*	-18.695	*3,9,15,18*	14.782	*4,10,14,17*	6.126
46	*3,9,14,20*	-19.351	*3,9,15,19*	15.025	*4,10,15,17*	6.212
47	*3,9,15,20*	-20.013	*4,10,15,18*	15.266	*4,10,15,18*	6.297
48	*3,9,15,21*	-20.680	*4,10,15,19*	15.506	*4,10,16,18*	6.381
49	*3,9,15,22*	-21.352	*4,10,16,19*	15.744	*4,10,16,19*	6.465
50	*4,10,15,21*	-22.029	*4,10,16,20*	15.981	*1,6,11,16,16*	6.547